Highlights

Observation of sporadic E layer altitude partially modulated by the Traveling Ionospheric Disturbances at high latitudes over Zhongshan station.

Alicreance HIYADUTUJE,Michael J. Kosch,John Bosco Habarulema,Xiangcai Chen,Judy A. E. Stephenson,Tshimangadzo Merline Matamba,Mpho Tshisaphungo

- Traveling Ionospheric Disturbances introduce a local polarization electric field in additional to the ionospheric background electric field.
- Es-layer altitude modulation observed by the ionosonde and estimated ion vertical drift at high-latitudes have a strong correlation.
- The MSTID polarization electric field contributes to the Es-layer altitude modulation through $\mathbf{E} \times \mathbf{B}$ drift mechanism.

Observation of sporadic E layer altitude partially modulated by the Traveling Ionospheric Disturbances at high latitudes over Zhongshan station.

Alicreance HIYADUTUJE[a,*], Michael J. Kosch[a,b,c], John Bosco Habarulema[a,d,e], Xiangcai Chen[f,g], Judy A. E. Stephenson[b], Tshimangadzo Merline Matamba[a] and Mpho Tshisaphungo[a]

[a] *South African National Space Agency (SANSA), Hermanus, South Africa*
[b] *Department of Chemistry and Physics, University of KwaZulu Natal (UKZN), Durban, South Africa*
[c] *Department of Physics, University of Lancaster, UK*
[d] *Department of Physics and Electronics, Rhodes University (RU), Makhanda, South Africa*
[e] *Centre for Space Research, Physics Department, North-West University, 2520, Potchefstroom , South Africa*
[f] *MNR Key Laboratory for Polar Science, Polar Research Institute of China, Shanghai, China*
[g] *Antarctic Zhongshan Ice and Space Environment National Observation and Research Station, Polar Research Institute of China, Shanghai, China*

ARTICLE INFO

Keywords:
MSTIDs
neutral wind
background electric field
polarization electric field
sporadic E layer
altitude modulation

ABSTRACT

At Zhongshan (69° S, 76° E) Antarctica we investigate the sporadic E (Es)-layer virtual height modulation, observed by an ionosonde, during the passage of the Medium-Scale Traveling Ionospheric Disturbances (MSTIDs), observed by a SuperDARN radar. Two events were identified, on 04 October 2011 at 07:00 - 12:00 UT and 29 February 2012 at 00:00 - 04:00 UT with periods of ∼15.0 and ∼12.0 min, respectively. The magnitude of average height modulation of the Es-layer was ∼10.4 ± 6.7 and ∼3.9 ± 3.4 km, respectively, with the same periods as the MSTIDs. Ray tracing during the events shows that the likely MSTID propagation was up to ∼300 km in the ionospheric F-region. The computed ion vertical drift velocity using SuperDARN radar and magnetometer data, and Es-layer altitude modulation observed by the ionosonde have moderate to strong positive correlation of 7.1 ± 0.22 and 0.51 ± 0.16, respectively. We show that the MSTIDs polarization electric field, which is mapped down from the F-region along the near-vertical magnetic field, moderately contributes to the modulation of the Es layer altitude via the $\mathbf{E} \times \mathbf{B}$ drift mechanism.

1. Introduction

Sporadic E (Es) layers are thin layers of enhanced plasma in the ionospheric E-region (∼90 - ∼150 km altitude) that have higher densities compared to the normal E-region density (Gubenko and Kirillovich, 2019). The real source of Sporadic E (Es)-layers is still unknown, but there is literature suggesting different mechanisms that are behind the formation of these thin layers (Mathews, 1998; Kirkwood and Nilsson, 2000). Some of the suggested mechanisms to create Es layers include Planetary Waves (PW) (Pancheva et al., 2003) and during Sudden Stratospheric Warming (SSW) events by reversing the zonal wind that affects the propagation of lunar tides (Liu et al., 2021). Es layers may be formed by the metal ions through the neutral wind shear instabilities (Kirkwood and Collis, 1989; Kirkwood and Nilsson, 2000; Gubenko and Kirillovich, 2019) caused by the divergence in the field-aligned ion velocity (downward and upward due to the atmospheric tidal motion), meteor ablation (Clemesha et al., 1988), particle precipitation, and internal

* Sporadic Es-layer altitude modulation

*Corresponding author
hiyadutujea@yahoo.fr (A. HIYADUTUJE)
ORCID(s): 0000-0002-3391-8737 (A. HIYADUTUJE); 0000-0003-2846-3915 (M.J. Kosch); 0000-0002-9716-7688 (J.B. Habarulema); 0000-0002-6325-5049 (X. Chen); 0000-0002-3840-7979 (J.A.E. Stephenson); 0000-0002-3466-7933 (T.M. Matamba); 0000-0002-5407-633X (M. Tshisaphungo)

gravity waves (Kirkwood and Collis, 1989; MacDougall et al., 2000; Gubenko and Kirillovich, 2019). Local electric field fluctuations were also found to be the source of these thin ionization layers (Kirkwood and Collis, 1989; Wahlund and Opgenoorth, 1989; Wahlund et al., 1989). Strong electric field associated with thunderstorms/lightning may give rise to the Es layers (Davis and Johnson, 2005). Smoke particles are involved in the development of metallic-ion Es-layers and Sudden Sodium Layers (SSL) (Kirkwood and Von Zahn, 1991). The Es layers were found to be more common in summer than in winter (Kirkwood and Nilsson, 2000).

High-latitude Es-layers could be thick (several 10s of km) or thin (their thickness is much less than the atmospheric scale height) (Kirkwood and Nilsson, 2000; MacDougall et al., 2000). These layers could be slowly descending in altitude due to tidal wind shear and sometimes are seen at constant altitudes (∼100 km) (Von Zahn and Hansen, 1988; Kirkwood and Nilsson, 2000). A recent study shows that an Es-layer was observed descending in the ionospheric E-region by the digisonde and SuperDARN radar at Zhongshan in Antarctica (Chen et al., 2022).

Gubenko and Kirillovich (2019) showed that in the Earth's high-latitude ionosphere, Es-layers were modulated by small-scale atmospheric waves. From the inclinations of horizontal Es layers at $h' =$ 95 - 133 km, they estimated some characteristics of the internal atmospheric waves. They found that their horizontal wavelengths were between 17.9 and 40.0 km. Mathews (1998) reviewed the Es-layers' latitude and found that they have horizontal quasi-periodic structures with 10 - 100 km scale. Other studies show that AGWs may modulate Es-layer within 95 - 140 km altitude (Woodman et al., 1991; Tsunoda et al., 1994; Huang and Kelley, 1996; Ogawa et al., 1998; Bernhardt, 2002; Yokoyama et al., 2004; Gubenko and Kirillovich, 2019). Es-layers altitude were modulated by AGWs within an amplitude of $< \sim\pm$ 15 km in the E-region (Woodman et al., 1991; Huang and Kelley, 1996; Ogawa et al., 1998; Bernhardt, 2002; Yokoyama et al., 2004; Gubenko and Kirillovich, 2019). Tsunoda et al. (1994) used the middle and upper atmosphere (MU) radar to show that Es-layers could have been modulated in altitude by the polarization electric field due to AGWs at ±7 and ±14 km in the mid-latitude region. Huang and Kelley (1996) and Ogawa et al. (1998) found that the AGWs may modulate the Es-layers with ∼10 km in altitude. Bernhardt (2002) found small amplitude modulation of ±200 m by the Kelvin-Helmholtz instability.

In the ionosphere, the TIDs are oscillating perturbations or waves propagating through its plasma. In most cases, they are generated by atmospheric gravity waves (AGWs) or the Perkins instability (Hunsucker, 1982; Miyoshi et al., 2018). Other mechanisms that can lead to the generation of TIDs are Joule heating, Lorentz force, earthquake, tsunami, tornado, volcanic eruption, thunderstorms, etc (Hunsucker, 1982; Hocke et al., 1996; Galushko et al., 1998; Liu et al., 2000; Snively and Pasko, 2003; Artru et al., 2005; Mikumo et al.; Ripepe et al., 2010; Heale et al., 2020; Shinbori et al., 2022; Kundu et al., 2022; Thaganyana et al., 2022; Van Eaton et al., 2023).

TIDs are observed by the SuperDARN radars in the slant far ranges. TIDs are grouped into small scale TIDs (SSTIDs), medium scale TIDs (MSTIDs) and large scale TIDs (LSTIDs) (Francis, 1974; Hunsucker, 1982; Hocke et al., 1996; Thaganyana et al., 2022). Their horizontal phase velocity (v), wavelength (λ), period (T), and propagation direction have been estimated (He et al., 2004; Grocott et al., 2013). SSTIDs have $\sim 300 \leq v \leq \sim 3000$ m/s, $0.3 \leq \lambda \leq 15$ km, $\sim 2 \leq T \leq \sim 5$ min (Hunsucker, 1982; Yin et al., 2019). The T, v, and λ are between ∼10 min and ∼1 hr, 100 and 300 m/s, of several hundred kilometers for MSTIDs, and 30 min and 3 hrs, 400 and 1000 m/s, > 1000 km for LSTIDs (Hocke et al., 1996; Sieradzki and Paziewski, 2015).

TIDs have an oscillating horizontal polarization electric field in the direction of propagation that is mapped down along the magnetic field lines (Otsuka et al., 2004; Kotake et al., 2007; Otsuka et al., 2007, 2009). It was found that this polarization electric field could be mapped from the F-region at the TIDs altitude to partially modulate the E-region Gradient Drift (GDI) and Farley-Buneman Instabilities (FBI) (Hiyadutuje et al., 2022, 2024). There are many other studies that reported the E- and F-region coupling where Es-layer polarization electric field was mapped into the F-region to generate the MSTIDs though instabilities (Tsunoda and Cosgrove, 2001; Cosgrove and Tsunoda, 2004; Cosgrove et al., 2004; Cosgrove, 2007; Otsuka et al., 2008; Yokoyama et al., 2008; Swartz et al., 2009; Yokoyama et al., 2009; Shalimov and Kozlovsky, 2015; Narayanan et al., 2018; Ejiri et al., 2019; Andoh et al., 2020; Cheng et al., 2021; Sivakandan et al., 2022; Fu et al., 2023). The majority of them reported the low- and mid-latitude events, but also there are a few similar studies at high-latitude and conjugate regions. Note that not all TIDs are electrified in nature (Paulino et al., 2016; Rathi et al., 2022). Coupling between the Es-layer and the F-region TIDs takes place only when the observed TIDs are electrified in nature.

In this study we have investigated the role that could be played by the MSTID polarization electric field in contributing to the Es-layer altitude modulation over the Zhongshan station (69° S, 76° E geographic coordinates) using SuperDARN HF radar, ionosonde and magnetometer data.

2. Instruments and models

2.1. Zhongshan SuperDARN High Frequency Radar

The TIDs in this study were observed by the Chinese SuperDARN HF radar located at Zhongshan 69.38°S, 76.38°E (74.9°S, 97.2°E magnetic coordinates). A SuperDARN radar's field of view (FOV) has 16 narrow beams, each beam covers an azimuth angle of $\sim 3.24°$ and which make up roughly 53° azimuth extent. Their operation frequencies fall between 8 and 20 MHz and all 16 beams are sounded within a dwell time of 3 or 7 s, every 1 or 2 minutes (Greenwald et al., 1995; Chisham et al., 2007). There are 75 range gates with a pulse length of 300 μs (i.e., each gate has 45 km) with the lag to the first range gate of 1200 μs, i.e., 180 km. The Zhongshan radar's operating frequency was 10.25 MHz, which means that irregularity of wavelength $\lambda \approx 14.6$ m were observed. The backscatter power and two (zonal and meridional) components of the background electric field are derived from the SuperDARN Doppler velocity which is the projection of the plasma convection velocity along a particular beam of the radar. The ionospheric plasma drift is $V_d = (\mathbf{E} \times \mathbf{B})/|B|^2$ and is derived from the SuperDARN measurements known as Doppler velocity in the plane perpendicular to $\mathbf{B}$ (Shepherd and Ruohoniemi, 2000; Chisham et al., 2007; Greenwald et al., 2008). The electrostatic potential (ϕ) can be expressed in terms of spherical harmonic functions depending on the magnetic co-latitude and longitude and $\mathbf{E} = -\nabla\phi$ (Ruohoniemi and Baker, 1998; Shepherd and Ruohoniemi, 2000; Chisham et al., 2007; Greenwald et al., 2008). The global convectional pattern is computed from the expansion and fitting of the velocity vectors. Where there is no backscatter, then a statistical convection model is used to constrain the potential (Ruohoniemi and Greenwald, 1996; Ruohoniemi and Baker, 1998; Shepherd and Ruohoniemi, 2000; Greenwald et al., 2008). The statistical convection model involves the solar wind electric field magnitude, Kp index, Interplanetary Magnetic Field (IMF) clock angle and dipole tilt angle. The current default version of the model is TS18 convection model (Thomas and Shepherd, 2018). Convection patterns and data are available on request (https://superdarn.thayer.dartmouth.edu/). The meridional and zonal components are the projections of the electric field vector into those two directions (Hiyadutuje et al., 2022). The electric field data is estimated in a 2 min cadence.

2.2. Zhongshan ionosonde

The Es-layers virtual heights are observed using the ionosonde data. The overhead ionosphere is monitored using the Digisonde Portable Sounder (DPS-4D) located at Zhongshan station (Li et al., 2007). It transmits and receives signals using a simple crossed delta antenna and four crossed magnetic dipole antennas, respectively. The DPS-4D at Zhongshan operates with an altitude resolution of 2.5 km (Chen et al., 2021). The time resolution of the instrument between two consecutive ionograms is 7.5 min (Chen et al., 2021). The DPS-4D operates with 0.05 MHz frequency step from 0.5 to 9.5 MHz. The virtual height h' in km showing the position of Es-layers used in this study was extracted using the Standard Archiving Output (SAO) Explorer (http://umlcar.uml.edu/DIDBase/) version 3.5.3 (Li et al., 2021). The scaled profiles were computed using the Automatic Real-Time Ionogram Scaler with true height (ARTIST-5) software (Galkin and Reinisch, 2008). The electron density N_e in cubic centimeter at the altitude of the Es-layer can be estimated using $foEs$ in MHz (Qiu et al., 2021).

2.3. Zhongshan magnetometer

A chain of five magnetometers was built in 2009 by the Chinese Compact Atomic Magnetometer (CAM). A regular fluxgate magnetometer was installed at 69.37° S, 76.38° E geographic location in 2013. The data is sampled at the frequency between 1.5 and 25 Hz, with an amplitude resolution of 0.01 nT. It is monitored by the Institute of Geology and Geophysics (IGG), Chinese Academy of Sciences (CAS) and it provides the H, D, Z and F components (Ables and Fraser, 2005; Liu et al., 2016). The data is one minute resolution,

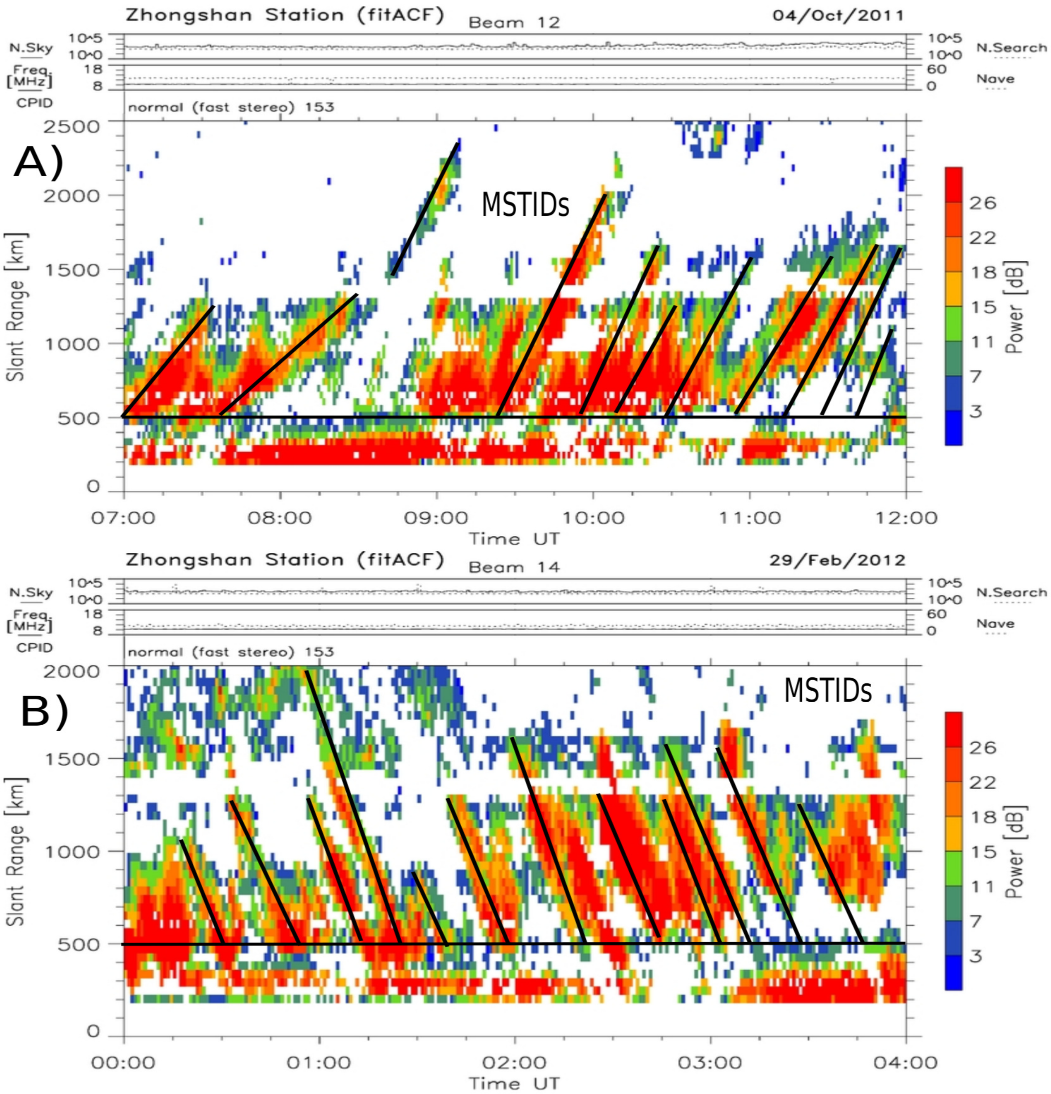

Figure 1: Range-time-intensity plot of backscatter power recorded from 07:00 to 12:00 UT on 04 October 2011 (A) and 00:00 to 04:00 UT on 29 February 2012 (B) using the Zhongshan radar beam 12 and 14, respectively.

but for a further analysis we have selected the data at 2 min intervals to match with the electric field data resolution.

2.4. Horizontal Wind and Mass Spectrometer Incoherent Scatter Models

The Horizontal Wind Model (HWM14) is used to estimate the zonal (U_X) and meridional (U_Y) components of the horizontal neutral wind (Drob et al., 2015). Since local thermospheric wind observations were not available, we use the Pyglow package (https://github.com/timduly4/pyglow) to get U_X and U_Y at

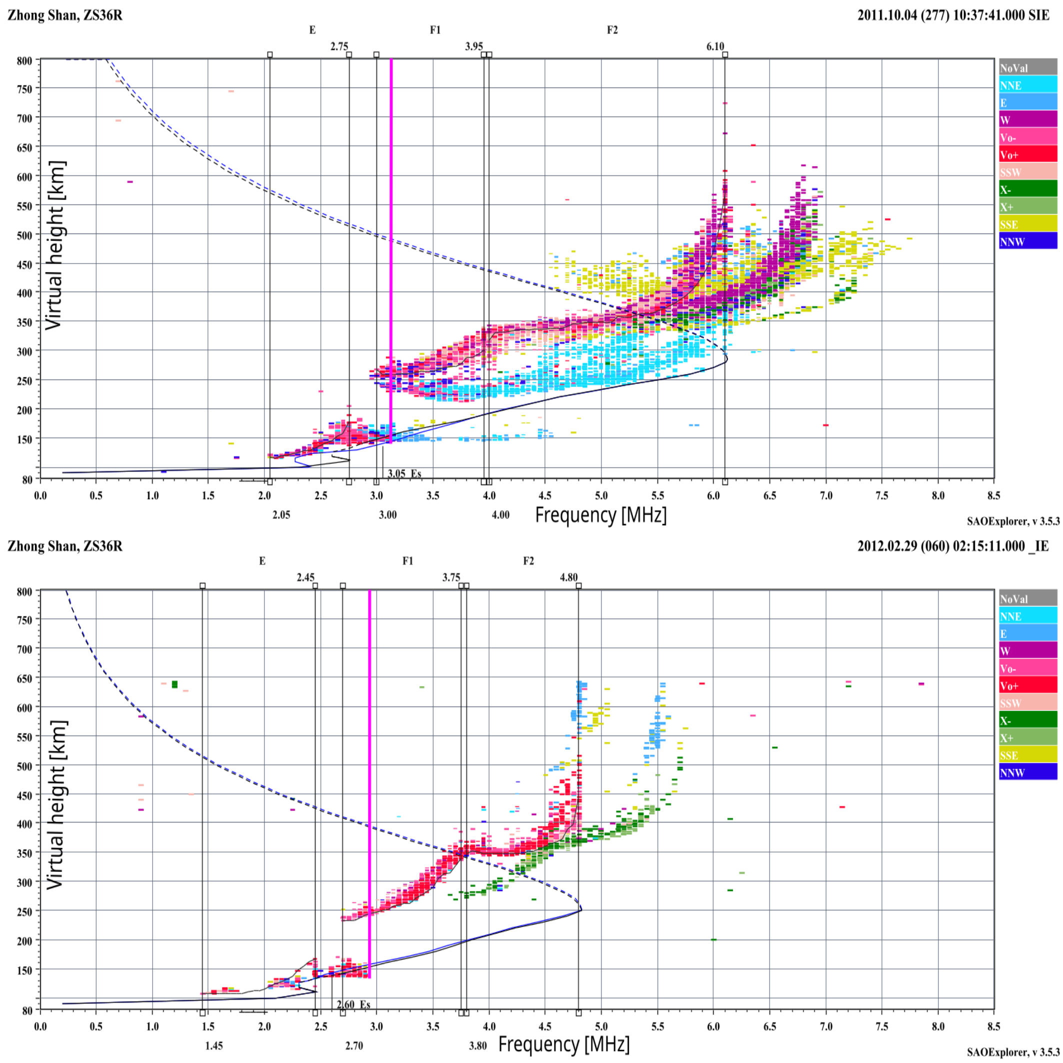

Figure 2: Examples of Es-layers observed by the Zhongshan digisonde were located at 138.0 and 133.3 km virtual height at around 10:37 (top panel) and 02:15 UT (bottom panel) on 04 October 2011 and 29 February 2012, respectively. The start of a vertical magenta line is added manually in each plot to show the foEs (along x-axis) and h$'Es$ (along y-axis). The automatic scaled Es-layer's virtual height and frequency are shown by the small black vertical line.

different altitudes of the E-region above the Zhongshan site.

The Naval Research Laboratory Mass Spectrometer Incoherent Scatter (NRLMSIS 2.0) model (Emmert et al., 2021) (https://ccmc.gsfc.nasa.gov/models/NRLMSIS 2.0/) is also used. NRLMSIS 2.0 model provides a number of outputs, but we used only Oxygen (O and O_2), Nitrogen (N_2) densities and neutral temperature (T_n). NRLMSIS 2.0 model is used to estimate the collisional frequencies between particles and neutrals at the altitudes of interest. The electron-neutral collision frequency is given by $\nu_e = 1.7 \times 10^{-11}[N_2]T_e + 3.8 \times 10^{-10}[O_2]\sqrt{T_e} + 1.4 \times 10^{-10}[O]\sqrt{T_e}$ (Pashin et al., 1995) while the ion-neutral collision frequency is given by $\nu_i = 4.34 \times 10^{-16}[N_2] + 4.28 \times 10^{-16}[O_2] + 2.44 \times 10^{-16}[O]$ (Schunk and Nagy, 2009). At each altitude below ~150 km in the E-region, we assume a quasi-neutrality and isothermal plasma, i.e., $n_i = n_e = n$ and

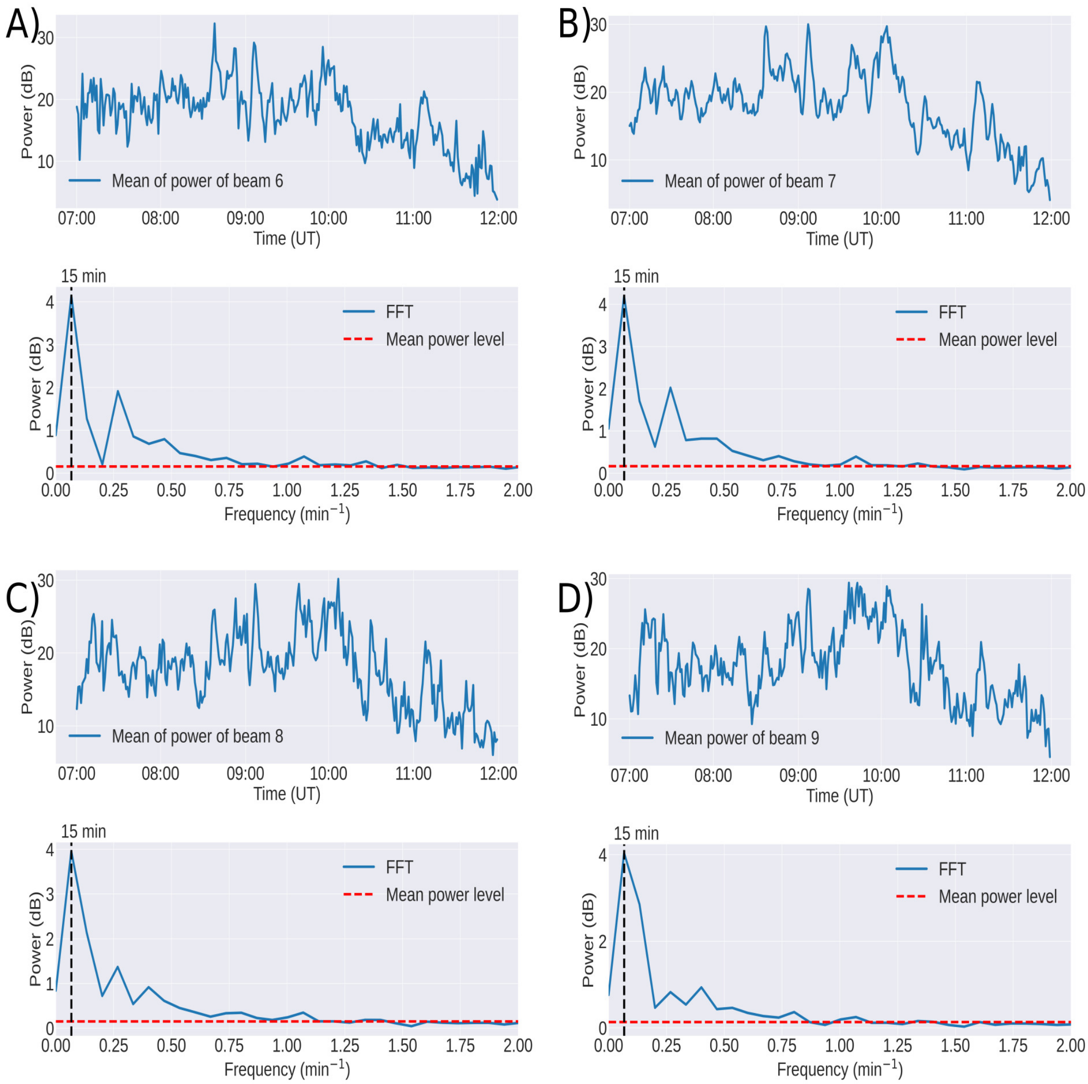

Figure 3: Average backscatter power and its fast Fourier transform (FFT) of far range gates (MSTIDs) of beam 6 (panel A), beam 7 (panel B), beam 8 (panel C) and beam 9 (panel D) of the Zhongshan HF radar on 04 October 2011 from 07:00 to 12:00 UT. All panels indicate that the dominant period of MSTIDs was ~15.0 min as shown in their time series FFT.

$T_i = T_e = T_n = T$, respectively (Bernhardt, 2002). Both models are empirical and were developed based on data that heavily relied on the northern hemisphere (NH) instrumentation.

3. Observation

3.1. MSTIDs and Es-layer observations

Figure 1 shows range-time-intensity (RTI) of backscatter power observed along beam 12 of the Zhongshan HF radar from 07:00 to 12:00 UT on 04 October 2011 (A) and beam 14 at 00:00 to 04:00 UT on 29 February 2012 (B). TIDs are clearly seen in the sloping quasi-periodic power enhancements that moves away from the radar (A) and toward the radar (B) with time at ranges of > 500 km. Periodic perturbations of backscatter power (dB) derived from the Zhongshan HF radar show the passage of TIDs over its beams. The propagation altitude of TIDs can be estimated based on the ray tracing tool. These TIDs were propagating in the F-region of the ionosphere at ∼200 - ∼300 km altitude (see appendix). Es-layers were observed simultaneously by the nearly vertical sounding ionosonde in the E-region between 95 and 140 km altitude. Figure 2 shows two manual scaled ionograms with the Es-layers at 138.0 and 133.0 km virtual heights with frequencies of 3.12 and 2.92 MHz as shown by the starting of magenta vertical lines, observed at Zhongshan at around 10:37 and 02:15 UT on 04 October 2011 (top panel) and 29 February 2012 (bottom panel), respectively. Other figures showing the Es-layers are presented in the supporting material. We notice that most of Es-layers in this study are similar to the one presented in Figure 14 (a3) by Chen et al. (2018). In some cases, Es-layer are spread in altitude indicating that instability or turbulent related to the electric field or gravity waves was affecting the wind shear in the aurora region where particle precipitation takes place (Resende et al., 2023). Spread-F that is present in both panels indicates that there were some wave activities such as TIDs in the ionospheric F-region.

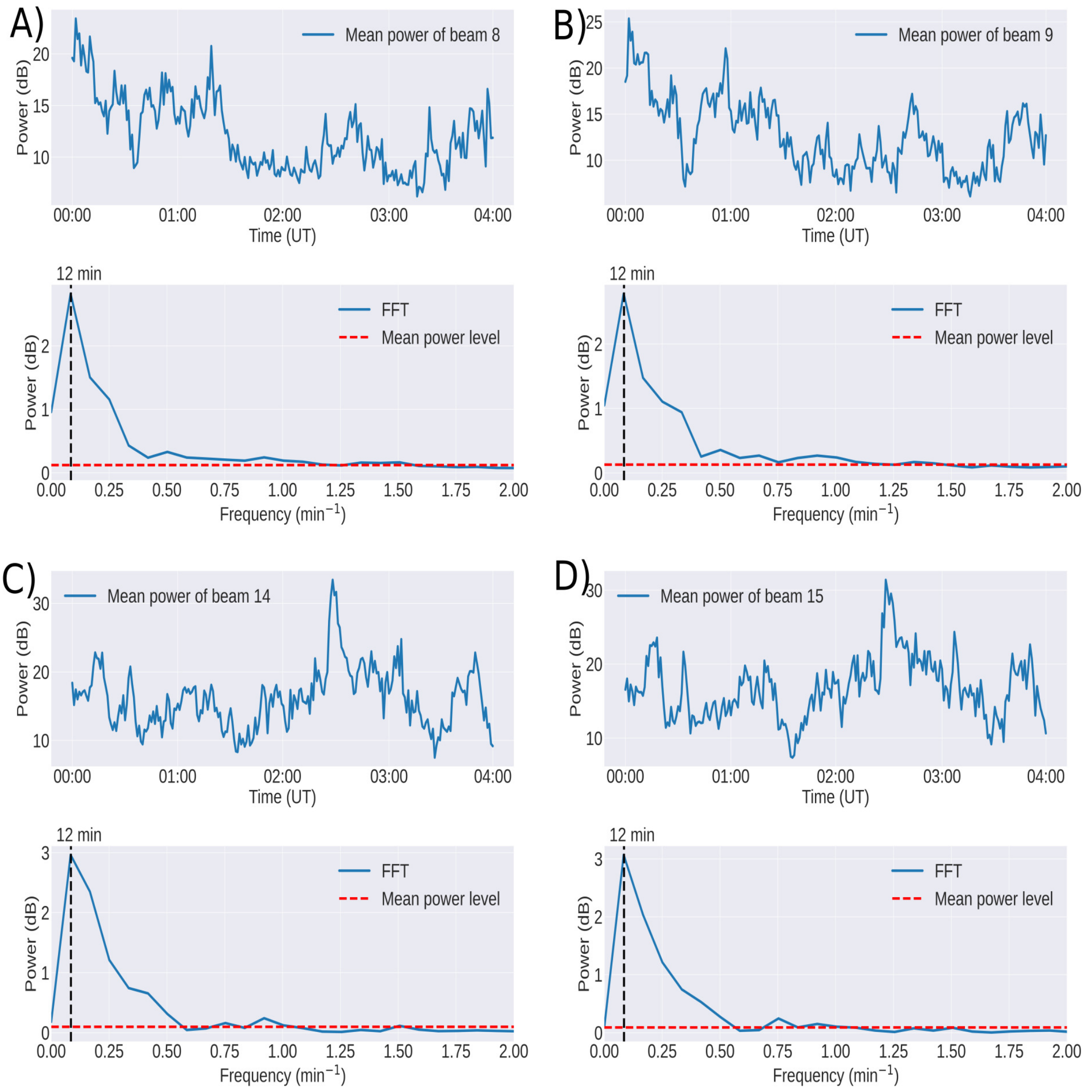

Figure 4: Average backscatter power and its FFT of far range gates (MSTIDs) of beam 8 (panel A), beam 9 (panel B), beam 14 (panel C) and beam 15 (panel D) of the Zhongshan HF radar on 29 February 2012 from 00:00 to 04:00 UT. All panels indicate that the dominant period of MSTIDs was ∼12.0 min as shown in their time series FFT.

3.2. MSTIDs characteristics

To find the characteristics of MSTIDs, we used the fast Fourier transform (FFT) cross-spectral analysis algorithm proposed by He et al. (2004). A set of three gates is used to estimate the phase differences and the dominant wavenumber within the set. The method used in this study was explained by Hiyadutuje et al. (2022), and an example of how the method was applied was shown in its supplementary material (S2). We present the summary of the important formulae used to find the MSTIDs characteristics (He et al., 2004). We have assumed that the MSTIDs were traveling horizontally in the F-region (He et al., 2004). After finding the dominant wavenumber along x- (k_x) and y-axis (k_y), the resultant wavenumber (k) can be estimated:

$$k = \sqrt{k_x^2 + k_y^2}. \tag{1}$$

Propagation azimuth angle (Az) was estimated by using:

$$Az = tan^{-1}\left(\frac{k_y}{k_x}\right), \tag{2}$$

taking into account the orientation of the radar's boreside angle (∼73°). We estimate the horizontal phase velocity (v) from the wavelength and the estimated period (T) of the MSTIDs,

$$v = \frac{\lambda}{T}, \tag{3}$$

where $\lambda = 2\pi/k$. Additionally, we produced movies of backscatter power over the radar's FOV to confirm the propagation direction (see supplementary material). The vertical oscillation (Francis, 1974) A in km of MSTIDs were estimated after assuming a cos-sinusoidal wave (Hiyadutuje et al., 2022). From the FFT showing the power frequency domain, we choose the dominant peak. The periods are consistent with the TID signature shown by the black oblique lines in Figure 1. The background noise is given by the mean power of the estimated FFT indicated by a dashed-horizontal red line (He et al., 2004) in Figure 3. Note that before applying the FFT, we subtract the mean of the backscatter power to remove the zero frequency component of the FFT. Figure 3 shows the average backscatter power and its FFT for the far range gates (> 500 km) of beam 6 (panel A), 7 (panel B), 8 (panel C) and 9 (panel D) of the Zhongshan HF radar on 04 October 2011 between 07:00 and 12:00 UT. We select the dominant peak showing period of ∼15.0 min on 04 October 2011 at 07:00 - 12:00 UT. MSTIDs parameters were the vertical oscillation of 83.8 km, azimuth direction of 106.0° (i.e., nearly eastward), phase velocity of 292.6 m/s and a period of 15 min. These parameters show that the disturbances were MSTIDs. Figure 4 is similar to Figure 3, but for the event on 29 February 2012 between 00:00 and 04:00 UT. We found that the periodicity in the average backscatter power received by the far range gates of beams 8, 9, 14, and 15 was ∼12.0 min. Other MSTID parameters were 77.0 km for the vertical oscillation, 278.5° azimuth angle (i.e., nearly westward) and phase velocities of 336.1 m/s.

Simultaneously, we observe the Es-layers using the ionosonde located at Zhongshan during the time when the MSTIDs were observed by the radar. For both cases, the Es-layer was observed moving up and down in time. All ionograms are attached separately in the supplementary material (see Figures 1 - 14 for the 04 October 2011 and 15 - 25 for the 29 February 2012 event). Altitude profiles manually scaled from the ionosonde data are presented to show the Es-layers modulation in Figure 5.

Figure 5 demonstrates the Es-layer modulation and shows that the layers could be linked with the above observed MSTIDs through their correlation (see the middle panels). We use beam 9 (b9) to find the correlation between the Es-layer virtual altitudes and the MSTIDs backscatter power. We choose beam 9 because TIDs can be observed by any single beam of the radar (He et al., 2004). Panels (a), (b) and (c) of Figure 5 show the Es-layer virtual altitude, normalized cross correlation (CC) between the Es-layer virtual heights and the respective backscatter power of beam 9, and FFT of h'Es, respectively on 04 October 2011 at 09:37 - 12:00 UT. The data between 07:00 and 09:37 UT are not used because Es-layer was only seen four times, hence there are long duration data gaps that can affect the estimated CC. Panels (d), (e) and (f) of the same figure are similar to panels (a), (b), and (c) for the event on 29 December 2012 at 00:00 - 04:00

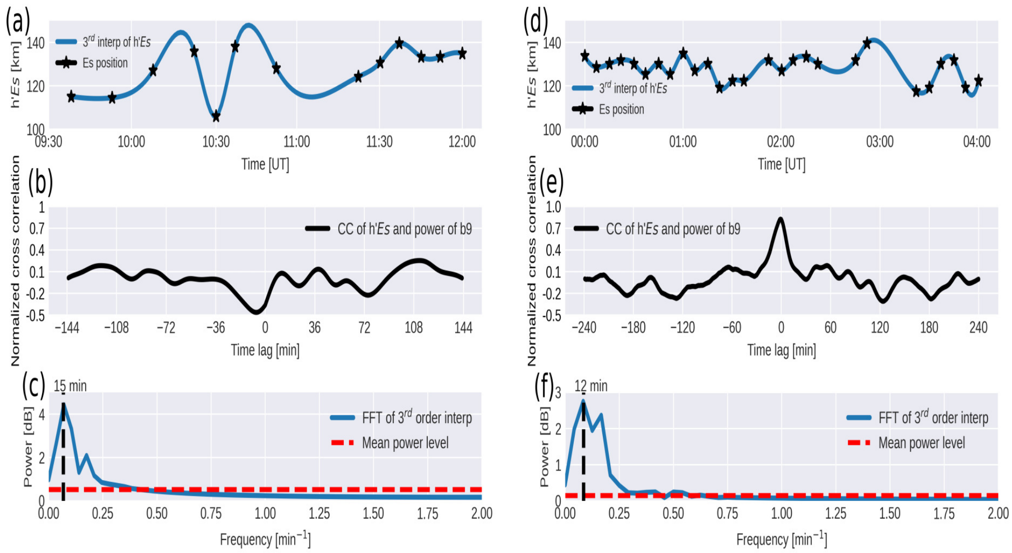

Figure 5: Panels (a), (b) and (c) show the Es-layer virtual altitude, normalized cross correlation (CC) between the interpreted Es-layer virtual heights and their FFT, respectively on 04 October 2011 at 09:37 - 12:00 UT. Panels (d), (e) and (f) are similar to panels (a), (b), and (c) for the event on 29 December 2012 at 00:00 - 04:00 UT. Their FFT plots in panels (c) and (f) show that their periods were 15.0 and 12.0 min, respectively.

UT. The middle panels show that the cross correlation coefficient peaks at ∼-0.46 (b) and 0.82 (e) meaning that there was a moderate and strong correlation, respectively. Periods are also found in the time series of the Es-layer virtual heights/altitudes. Their FFT plots in panels (c) and (f) show that their periods were 15.0 and 12.0 min, respectively, i.e., the same periods as the TIDs.

4. Method

At high latitudes, the motion of ions is governed by the neutral wind ($\mathbf{U}$), effective electric field ($\mathbf{E}^*$), particle interactions as well as the Earth's magnetic field ($\mathbf{B}$). Ambipolar diffusion and the force of gravity also play an important role in the ion motion. Kirkwood and Nilsson (2000), assuming a steady-state ion drift, plasma pressure gradients in one dimension (vertical), considered only ions as species and singly charged to derive the ion drift velocity. The ion drift velocities (v_{iz}) that result in Es-layers in the vertical direction are (adapted from papers by Kirkwood and Von Zahn (1991) and Kirkwood and Nilsson (2000)):

$$v_{iz} = \frac{\Omega_i^2}{\Omega_i^2+\nu_i^2}\left[\frac{E_X^*}{B}+U_Y\sin I\right]\cos I \tag{4a}$$

$$+\frac{\Omega_i\nu_i}{\Omega_i^2+\nu_i^2}\left[\frac{E_Y^*}{B}+U_X\right]\cos I \tag{4b}$$

$$+\left[1-\frac{\Omega_i^2\cos^2 I}{\Omega_i^2+\nu_i^2}\right]U_Z \tag{4c}$$

$$-\frac{\Omega_i\Omega_e}{\Omega_i\nu_e+\nu_i\Omega_e}\left[\frac{1}{n}\frac{d(nkT)}{dz}+mg\right]\frac{2}{eB}\left(\sin^2 I+\frac{\nu_i\nu_e\cos^2 I}{\nu_i\nu_e+\Omega_i\Omega_e}\right), \tag{4d}$$

where Ω_α and ν_α are the gyro and collision frequencies of species ($\alpha = i, e$), respectively (Kirkwood and Von Zahn, 1991; Kirkwood and Nilsson, 2000). The subscripts i and e indicate ions and electrons. Other symbols E_β, B, U_μ, k, T, n, e, m, g and I are components of electric field ($\beta = Y, X$), the total magnetic field of the Earth, components of the neutral wind ($\mu = Y, X, Z$), Boltzmann's constant, the plasma temperature, plasma density, electron charge, ion mass, acceleration due to gravity and magnetic inclination, respectively.

For the horizontal Es layer, the horizontal ion motion might affect its height variation due to the inclination of the magnetic field. Figure 6 shows a geographic coordinates cartoon of the vertical, eastward (zonal) and

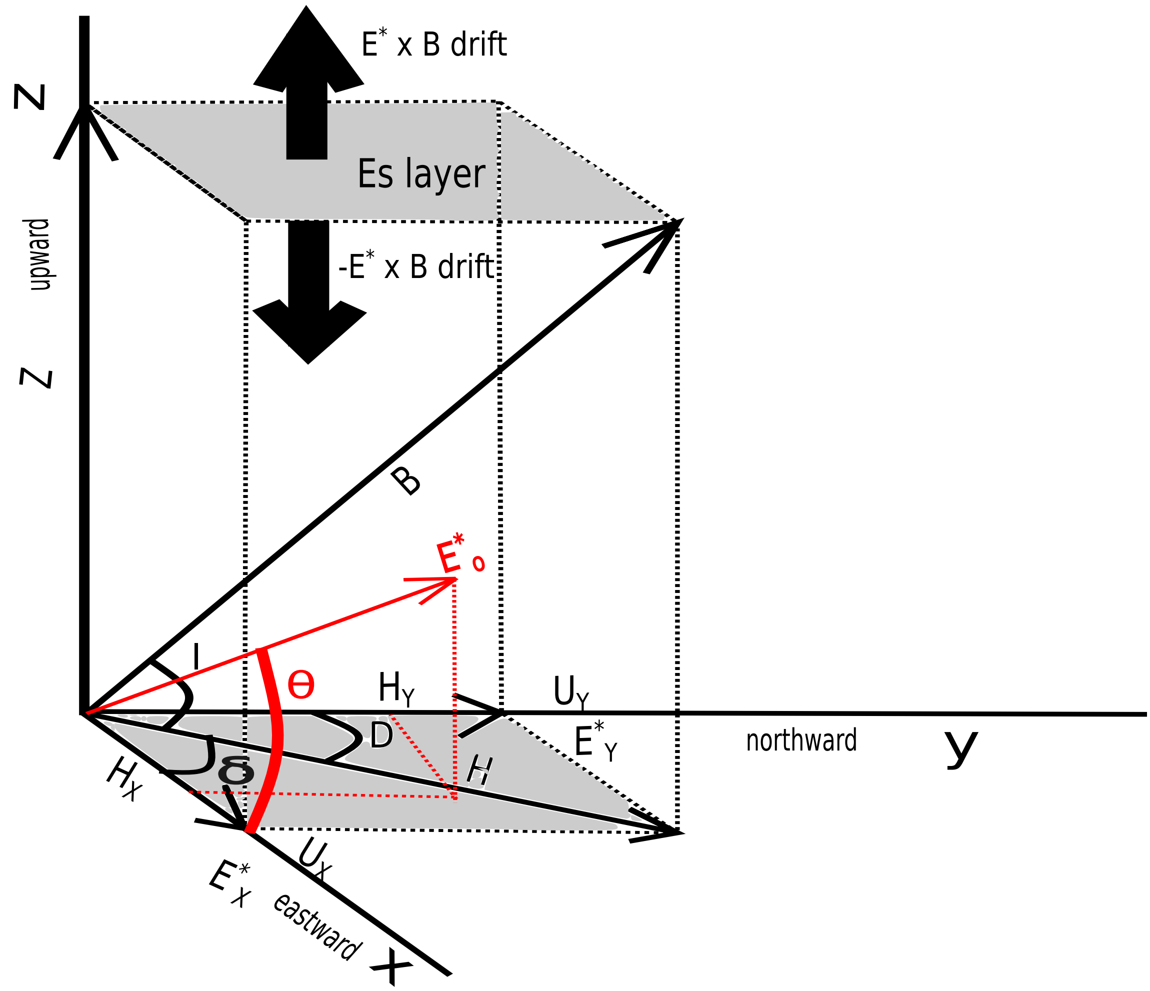

Figure 6: Geomagnetic and electric field components in the southern hemisphere. The $\mathbf{Z}$, $\mathbf{H_Y}$, and $\mathbf{H_X}$ component of $\mathbf{B}$ is negative upward, positive northward, and positive eastward, respectively. The red arrow shows the total electric field due to the background electric field and the wind dynamo ($\mathbf{E_o^*} = \mathbf{E_o} + \mathbf{U} \times \mathbf{B}$). The components of the effective electric field ($\mathbf{E}^* = \mathbf{E_o^*} + \delta\mathbf{E_P}$), $\mathbf{E_X^*}$ and $\mathbf{E_Y^*}$ are along x- and y-axis, respectively. The horizontal and total intensity of the magnetic field is H and B, respectively. Meridional ($\mathbf{U_Y}$ and $\mathbf{E_Y}$) and zonal ($\mathbf{U_X}$ and $\mathbf{E_X}$) components of neutral wind and electric field, respectively are presented. The $\mathbf{E} \times \mathbf{B}$ drift would push the Es-layer upward and downward, respectively.

northward (meridional) components of $\mathbf{B}$ and $\mathbf{E_o^*} = \mathbf{E_o} + \mathbf{U} \times \mathbf{B}$ in the southern hemisphere. Note that $\mathbf{E_o}$ is the background electric field generated by the F-region dynamo (Otsuka, 2021). The magnetic field components $\mathbf{Z}$ and $\mathbf{H}$ and their resultant $\mathbf{B}$ are presented, where $\mathbf{H}$ can be projected along x- and y-axis to give $\mathbf{H_X}$ and $\mathbf{H_Y}$, respectively. Two horizontal neutral wind $\mathbf{U_X}$ and $\mathbf{U_Y}$ and electric field $\mathbf{E_X}$ and $\mathbf{E_Y}$ components are also shown. The symbols I and D represent the magnetic inclination and declination angles, respectively.

The first term of the equation 4, (4a) plays an important role above 120 km altitude where $\Omega_i >> \nu_i$ (Kirkwood and Nilsson, 2000). Ions flow partially in a direction perpendicular to both the electric and magnetic field directions due to the $\mathbf{E} \times \mathbf{B}$ drift caused by the zonal component of the electric field (Kirkwood and Von Zahn, 1991). Note that the ions flow direction will take the direction of the meridional wind into consideration (Kirkwood and Von Zahn, 1991). The second term of the equation 4, (4b) significantly contributes to the ion motion at the altitude below 110 km where $\nu_i >> \Omega_i$ (Kirkwood and Nilsson, 2000). Vertical wind, zonal wind and the meridional electric field via $\mathbf{U} \times \mathbf{B}$ drift contribute to the vertical motion

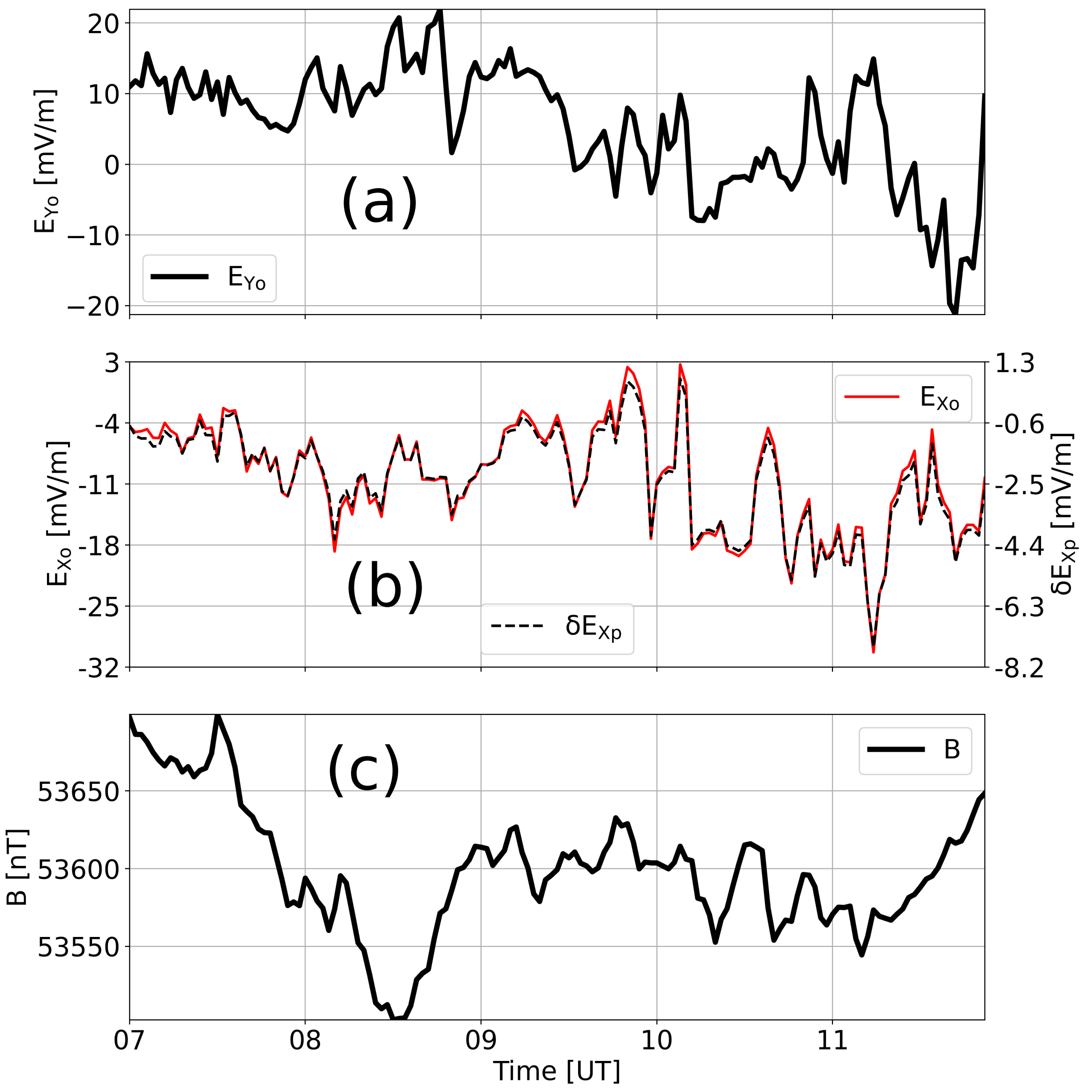

Figure 7: Time series plots of: (**a**) northward component of the ionospheric background electric field (E_{Yo}), (**b**) eastward component of the ionospheric background electric field (E_{Xo}) and the polarization electric field (δE_{Xp}), (**c**) the magnitude of total magnetic field on 04 October 2011.

of the ions (Kirkwood and Nilsson, 2000). The third term of the equation 4, (4c) is important at any altitude as long as there is a vertical motion, such as an AGW/TID (Kirkwood and Nilsson, 2000). It shows the motion of ions carried by the vertical wind component. A constant U_Z of an upward 50 m/s in magnitude is assumed (Rees et al., 1984) because we don't have the observations of the vertical thermospheric wind at Zhongshan for the duration of each of the two events in this study. The last term of the equation 4, (4d) represents the ion diffusion caused by the plasma pressure and the ion weight/gravity force (Kirkwood and Nilsson, 2000). This term plays an important role on a thick Es-layer such as those formed by aerosol particles.

Meridional and zonal components of the electric field, geomagnetic field, meridional and zonal neutral wind are derived from the SuperDARN radar network (see section 2.1), local magnetometer, and HWM14 model, respectively. Collision and gyro-frequencies were estimated using the NRLMSIS 2.0 model. All the parameters presented in equation (4) are substituted using observations where available to get the vertical ion drift velocity (v_{iz}) estimate. Using the background electric field and the horizontal neutral wind, the magnitude of MSTID polarization electric field can be estimated (Otsuka et al., 2007; Otsuka, 2021; Hiyadutuje et al., 2022). The MSTIDs produce polarization electric fields that are perpendicular to their wavefronts in the direction of travel (Otsuka, 2021). The polarization electric field ($\delta \mathbf{E_{pF}}$) is given by:

$$\delta \mathbf{E_{pF}} = \frac{\delta \Sigma_p}{\Sigma_p}\left(\mathbf{E_o} + \mathbf{U} \times \mathbf{B}\right) \cdot \frac{\mathbf{k}}{|\mathbf{k}|} = \frac{\delta \Sigma_p}{\Sigma_p}\left(E_o^*\right) \cdot \frac{\mathbf{k}}{|\mathbf{k}|} = \frac{\delta \Sigma_p}{\Sigma_p}\left[E_o^* \cos(\beta - \alpha)\right] \tag{5}$$

where $\mathbf{U}$ is the neutral wind velocity, $\mathbf{k}$ is the wave vector of MSTID and $\delta \mathbf{E_{pF}}$ is generated within a MSTID wave to maintain divergence-free Pedersen current continuity ($\mathbf{J} = \Sigma_p(\mathbf{E_o} + \mathbf{U} \times \mathbf{B})$) (Otsuka et al., 2004, 2007, 2009; Otsuka, 2021; Zhang and Paxton, 2021). β is the angle between $\mathbf{E_o^*}$ and the geographic east while α is the angle between $\mathbf{k}$ and the east (Otsuka, 2021). Note that Σ_p is the field line-integrated Pedersen conductivity, $\delta\Sigma_p$ is its perturbation due to the MSTID waves. Dividing $\delta\Sigma_p$ with Σ_p ($\delta\Sigma_p/\Sigma_p$) leads to the perturbation percentage of the background electric field due to the MSTIDs (Otsuka et al., 2009; Hiyadutuje et al., 2022). $\delta\Sigma_p$ and Σ_p are estimated using the ionospheric conductivity model (height profile) (https://wdc.kugi.kyoto-u.ac.jp/ionocond/exp/icexp.html) based on the TID vertical oscillations. For details on the Pedersen conductivity and its perturbation estimation during the MSTID, see sub-section 5.1 below. This method was also used by Hiyadutuje et al. (2022).

Equation (5) can be rearranged to estimate the δE_{pF} in the eastward direction (δE_{XpF}) by considering the background eastward electric field (E_{Xo}) and polarization electric field due to the meridional neutral wind. First, we estimate the total electric field ($\mathbf{E_o^*}$) generated by the background electric field and the neutral wind dynamo;

$$E_o^* = \sqrt{(E_{Xo} + UB_X)^2 + (E_{Yo} + UB_Y)^2 + (UB_Z)^2} = \sqrt{(E_{Xo}^*)^2 + (E_{Yo}^*)^2 + (E_{Zo}^*)^2} \tag{6}$$

where the components of the $\mathbf{U} \times \mathbf{B}$ in three dimension are: $UB_X = U_Y \cdot Z - U_Z \cdot H_Y$, $UB_Y = U_Z \cdot H_X - Z \cdot U_X$ and $UB_Z = U_X \cdot H_Y - Z \cdot U_Y$. From the equations (5) and (6), the eastward polarization electric field due to the MSTIDs can be estimated:

$$\delta E_{XpF} = \frac{\delta \Sigma_p}{\Sigma_p} E_o^* \cos(\theta) \tag{7}$$

where $\theta = \beta - \alpha$ is the angle between $\mathbf{E_o^*}$ and $\mathbf{k}$ (Otsuka, 2021), the factor $\cos(\theta) = E_{Xo}^*/E_o^*$ (see Figure 6). For both events, the deviation of the MSTIDs azimuth angle from the east/west is small, we assume that $\alpha \approx 0$. $\mathbf{U_Y}$ and $\mathbf{U_X}$ are the meridional and zonal neutral wind from the HWM14 at ~300 km altitude (MSTIDs are considered to propagate at this altitude) based on the ray tracing model output (see Figure 11 in section 7 (appendix)). A strong electric field coupling between the E- and F-region exists since the magnetic field is assumed to be equipotential. Between the Es-layers and MSTIDs altitudes, the distance is only a few hundreds of kilometers. The electric field would be mapped down to the E-region along the magnetic field lines ($\delta \mathbf{E_{XpF}} = \delta \mathbf{E_{XpE}}$) (Otsuka et al., 2004; Hiyadutuje et al., 2022) and contribute to the altitude modulation of the existing Es-layer. On the other hand, the Es-layer polarization electric field would be mapped from E- to F-region to generate the ionospheric irregularities, such as spread-F, TIDs, etc (Haldoupis et al., 2003; Kelley et al., 2003). We assume the Es-layer polarization electric field of $0.1E_{Xo}$ (Tsunoda et al., 1994) and add it to the background and MSTID polarisation electric fields to estimate the modulation amplitude. Zonal and meridional components of the effective electric field $\mathbf{E}^*$ used in equation (4) are $E_X^* = E_{Xo}^* + \delta E_{XpE} + 0.1E_{Xo}$ and $E_Y^* = E_{Yo}^*$.

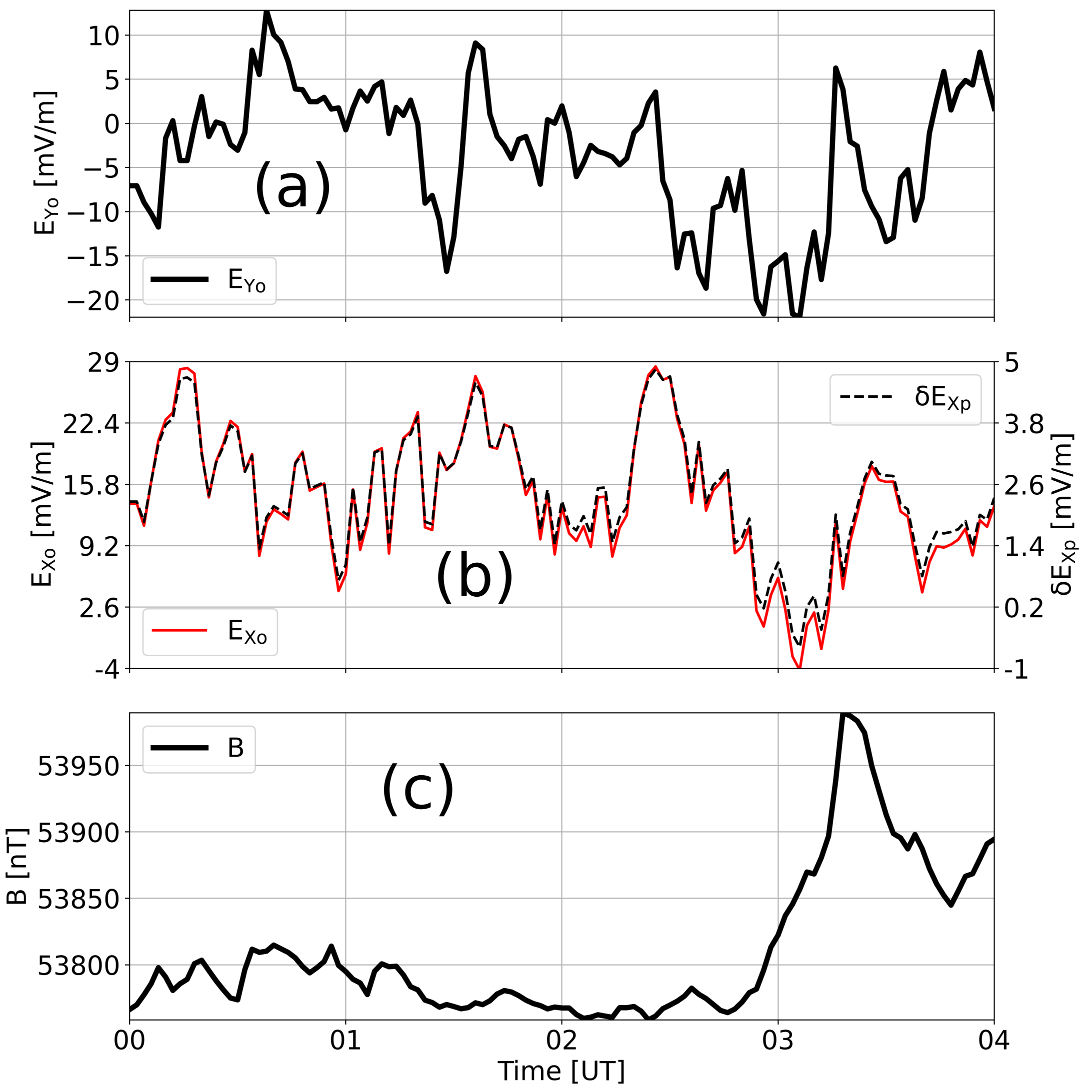

Figure 8: Time series plots of: (**a**) northward component of the ionospheric background electric field (E_{Yo}), (**b**) eastward component of the ionospheric background electric field (E_{Xo}) and the polarization electric field, (**c**) the magnitude of total magnetic field on 29 February 2012.

5. Results and discussion

5.1. MSTID polarization electric field during the events on 04 October 2011 and 29 February 2012

We have plotted the total magnetic field and both electric field components for the two events used to estimate v_{iz} in equation (4). Figures 7 and 8 show the time series plots of (a) the meridional component of the ionospheric electric field (E_{Yo}), (b) the zonal component of the ionospheric electric field (E_{Xo}) in a red line and δE_{XpF} or simply δE_{Xp} in a black dashed line, and (c) B, at 07:00 - 11:52 UT on 04 October 2011 and 00:00 - 04:00 UT on 29 February 2012, respectively.

Figure 7 (a) shows E_{Yo} with a magnitude fluctuating between -20 and 20 mV/m. From 07:00 to 09:30 UT, E_{Yo} was northward and at 09:30 - 11:52 UT E_{Yo} was fluctuating between northward and southward.

The ratio $\delta\Sigma_p/\Sigma_p$ in equation (7) was estimated by taking the difference between the height-integral of Pedersen conductivity at (300 + A) km and at (300 - A) km altitudes over the total Pedersen conductivity (see the model in section 4). A is the vertical oscillation of the MSTIDs (Francis, 1974). For the event on 04 October 2011, A = 83.8 km we estimate $\delta\Sigma_p/\Sigma_p \approx 14.4\%$. Figure 7 (b) shows the fluctuated westward ionospheric electric field with magnitude between -32 and ~3 mV/m. It also shows the δE_{Xp} with the same trend as the E_{Xo} between ~-8.0 and ~1.0 mV/m. These values agree well with the previous studies, where the background electric field is perturbed by ~10% (Zhang et al., 2001; Hiyadutuje et al., 2022). Otsuka et al. (2007) estimated the MSTID polarization electric field to be 1.1 mV/m using airglow imager. Figure 7 (c) presents the total Earth's magnetic field (B). Figure 8 (a) shows the E_{Yo} fluctuating mostly in southward between ~-20 and ~10 mV/m. $\delta\Sigma_p/\Sigma_p$ in equation (7) was estimated to be 6.6% on 29 February 2012. The E_{Xo} in dashed black line was fluctuating mostly eastward between ~-4 and ~30 mV/m while δE_{Xp} in thin red line was between ~-1.0 and ~5.0 mV/m as shown in panel (b). Panel (c) shows the total Earth's magnetic field B during this event.

The auroral electrojet (AE) index of ~500 and ~400 nT show that substorms may have taken place during the 2011 and 2012 events, respectively (Yenen et al., 2015). SYM-H reached ~-22 and ~-30 nT while Kp index reached +2 and +3, respectively indicating that a minor storm could have taken place during the 29 February 2012 event.

5.2. MSTID contribution to the Es-layer altitude modulation

We have estimated the magnitude of δE_{XpE} using equation (7) while B is measured by the magnetometer. The $\mathbf{E}^* \times \mathbf{B}$ drift, $\mathbf{V'_{Es}}$ which involves the MSTIDs polarization electric field in the Es-layer altitude modulation can be estimated using equation (8);

$$\mathbf{V'_{Es}} = \frac{\mathbf{E}^* \times \mathbf{B}}{|B|^2} = \frac{\mathbf{E}^* \times (\mathbf{Z} + \mathbf{H})}{|B|^2} \tag{8}$$

where $\mathbf{E}^* = \mathbf{E_o^*} + \delta\mathbf{E_p}$, contribution of the $\mathbf{U} \times \mathbf{B}$ dynamo, the MSTIDs $\delta\mathbf{E_{Xp}}$ and Es-layer $0.1\mathbf{E_{Xo}}$ polarization electric fields. The components of the magnetic field are given by $\mathbf{Z} = \mathbf{B}\sin(I)$, $\mathbf{H} = \mathbf{B}\cos(I)$, $\mathbf{H_Y} = \mathbf{B}\cos(I)\cos(D)$ and $\mathbf{H_X} = \mathbf{B}\cos(I)\sin(D)$ (see Figure 6). We use the equation (4) to estimate the v_{iz} during the duration of each of the two events in this study since the contribution of both components of electric field and magnetic field on the v_{iz} were considered (Kirkwood and Von Zahn, 1991).

We remove the linear trend in the v_{iz} time series by subtracting the least-squares fit to the data from the original data (https://docs.scipy.org/doc/scipy/reference/generated/scipy.signal.detrend.html) and compute the altitude modulation ($\Delta\ h_{iz}$) by using 2 min corresponding to the data time step. The same method of removing the linear trend is used to find the $\Delta\ h'Es$ estimated from the $h'Es$. We have used equation (4) by considering the MSTID's contribution, i.e., E_{XpE}. Recall that the MSTID propagation directions were 106.0° and 278.5°, so essentially in the zonal direction only. The MSTID's polarization electric field in the northward/southward direction is very small, i.e., $E_{YpE} \approx 0$.

Figure 9 shows the Es-layer altitude ($h'Es$) from the ionosonde measurements and the estimated vertical component of ion drift velocities (v_{iz}) between 90 and 150 km altitudes on 04 October 2011. The top panel (**a**) shows the Es-layers altitude (black dots) and its standard deviation unit (error bars of ± 9.6 km), a third order polynomial interpolation (black line), estimated ion vertical drift velocities (dashed blue), selected ion drift velocities (blue dots) at the time when the Es-layers data were available, and a third order polynomial interpolation of those drift velocities shown by the blue line. The digisonde $h'Es$ uncertainty can be of the order of ~2 - 3 km (Haldoupis et al., 2024). The Es-layer virtual height (black dots) is seen between 105 and 140 km altitude. The ion drift velocities were estimated to be between ~7.3 and ~164.6 m/s with average of ~61.7 m/s. This value is close to the Es-layers vertical velocity of 100 m/s published by MacDougall et al. (2000). The third order polynomial interpolation is used to mimic other positions of Es-layer (black line) and velocities of ions (blue line) during the time interval when there was no Es-layer in the ionosonde data.

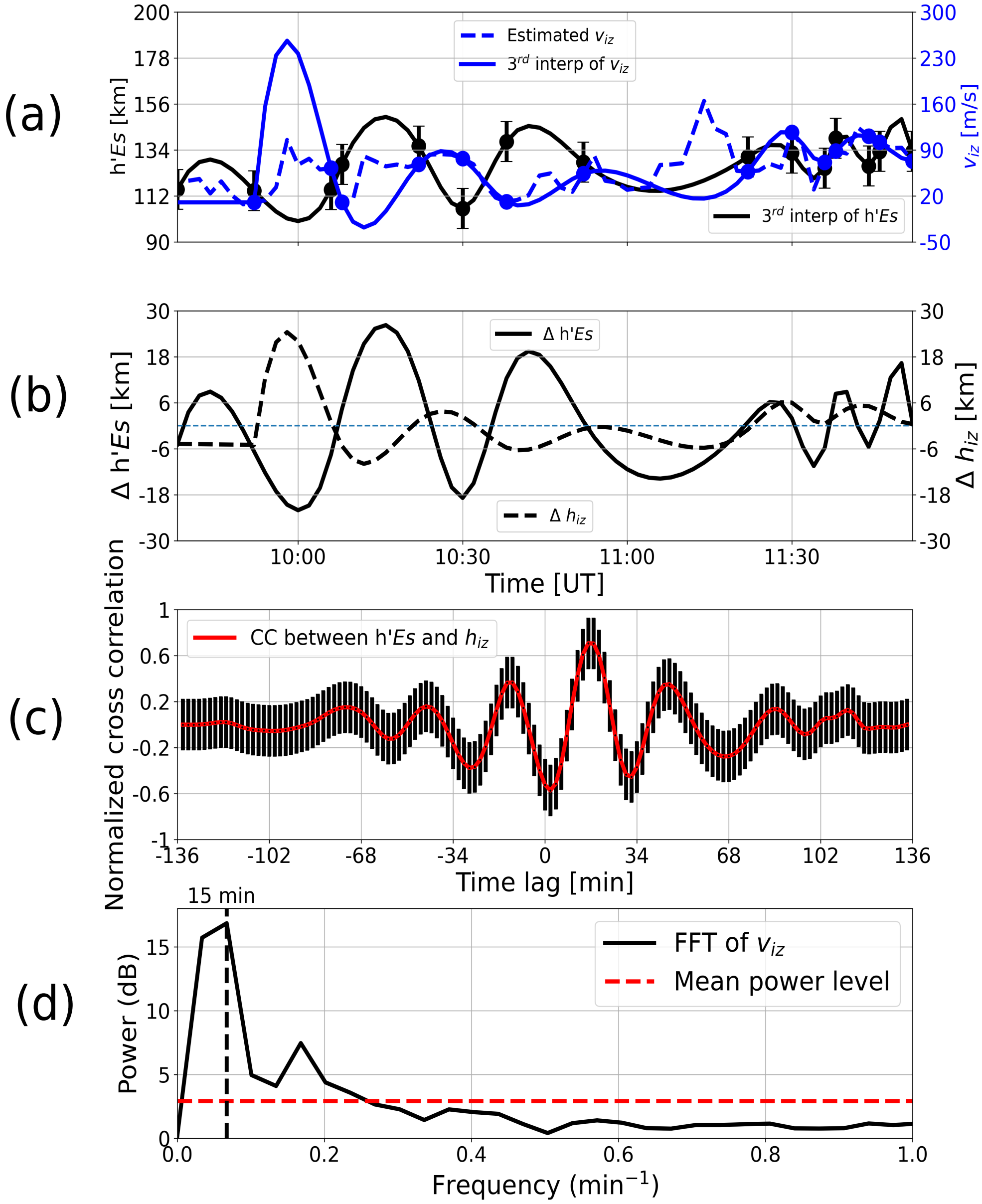

Figure 9: The Es-layer modulation on 04 October 2011. The top panel (**a**) shows the virtual height of the Es-layer ($h'Es$) and its standard deviation unit (black dots and error bars), a third order polynomial interpolation (black solid line), estimated vertical ion drift velocities (v_{iz}, blue dashed line), estimated ion drift velocities at the time when Es-layers data were available (blue dots), and the third order polynomial interpolation of those velocities (blue line) after every 2 min. Panel (**b**) shows the linear detrend of the interpolated observed Es-layer position ($\Delta\ h'Es$) (black solid line) and estimated altitude modulation ($\Delta\ h_{iz}$) (black dashed line). Panel (**c**) shows the CC between the interpolated observed Es-layer positions and estimated h_{iz}. The CC's error bars in black are equivalent to its standard deviation unit. The bottom panel (**d**) shows the FFT of v_{iz} with the dominant peak showing a period of ∼15 min.

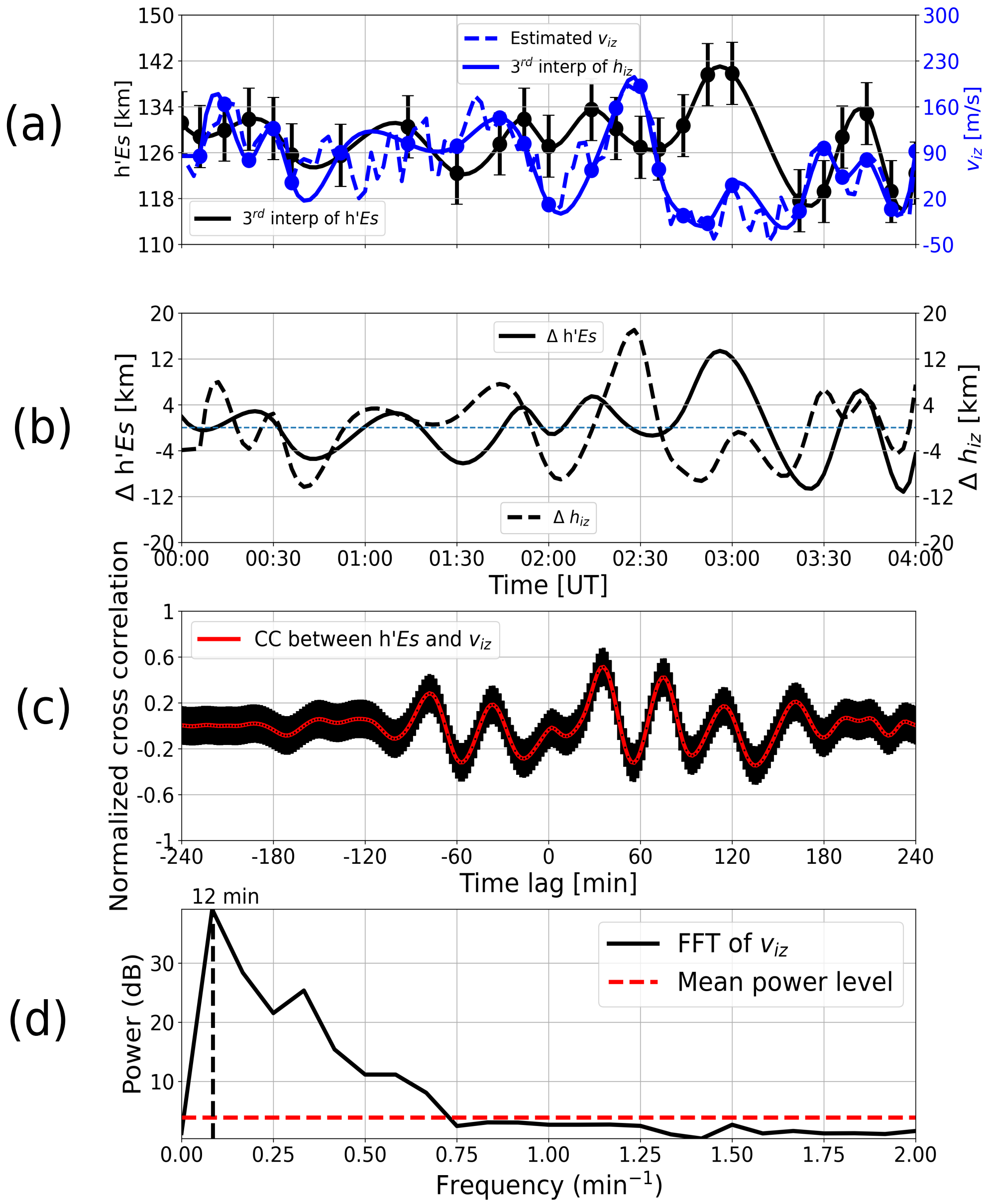

Figure 10: The Es-layer modulation on 29 February 2012. The top panel (**a**) shows the virtual height of the Es-layer ($h'Es$) and its standard deviation unit (black dots and error bars), a third order polynomial interpolation (black solid line), estimated vertical ion drift velocities (v_{iz}, blue dashed line), estimated ion drift velocities at the time when Es-layers data were available (blue dots), and the third order polynomial interpolation of those velocities (blue line) after every 2 min. Panel (**b**) shows the linear detrend of the interpolated observed Es-layer position ($\Delta\ h'Es$) (black solid line) and estimated altitude modulation ($\Delta\ h_{iz}$) (black dashed line). Panel (**c**) shows the CC between the interpolated observed Es-layer positions and estimated h_{iz}. The CC's error bars in black are equivalent to its standard deviation unit. The bottom panel (**d**) shows the FFT of v_{iz} with the dominant peak showing that the period was ∼12 min.

Panel (**b**) shows the Es-layer altitude modulation ($\Delta\ h'Es$) obtained from the ionosonde measurements and estimated altitude modulation ($\Delta\ h_{iz}$), respectively. The residual after removing the linear trend from the Es-layer altitudes and altitude modulation estimated from the ion drift velocities in panel (**a**) are plotted. The average of the observed Es-layers amplitude modulation ($\Delta\ h'Es$) is $\sim\pm$ (10.4 $\pm$ 6.7) km while the estimated average of the $\Delta\ h_{iz}$ amplitude is $\sim\pm$ (5.0 $\pm$ 4.8) km. The CC between $\Delta\ h'Es$ and $\Delta\ h_{iz}$ was also 0.71 $\pm$ 0.22. The bottom panel (**d**) shows the FFT estimated from v_{iz} shown in blue dashed line in panel (**a**). Clearly, the dominant peak similar to that in FFT estimated using the MSTID SuperDARN backscatter power in Figure 3 are evident in the Es-layer altitude modulation (see similar FFT peak in Figure 5(c)). This is unsurprising because δE_{XpE} must have the period of the TID by definition.

Figure 10 is similar to Figure 9, but for the 29 February 2012 event at 00:00 - 04:00 UT. The uncertainty in the observed Es-layers altitude was $\pm$5.4 km. The average of the observed Es-layers amplitude modulation is $\sim\pm$ (3.9 $\pm$ 3.4) km while the estimated average of the $\Delta\ h_{iz}$ amplitude is $\sim\pm$ (4.8 $\pm$ 3.5) km. The CC between $\Delta\ h'Es$ and $\Delta\ h_{iz}$ was 0.51 $\pm$ 0.16. The dominant peak shows that the period of the estimated v_{iz} was $\sim$12 min similar to that in FFT estimated using the MSTID Zhongshan HF radar backscatter power and Es-layer altitude modulation shown in Figures 4 and 5(f), respectively. Similar figures to Figures 9 and 10 obtained using the automatic scaling are presented in the supplementary material (see Figures 28 and 29). As seen in different ionograms, Figures 28 and 29 include Es-layers that are embedded in the ordinary E-region layers and sometimes the system doesn't differentiate the Es-layers and E-region layers. Nevertheless, the presented strong CC between $\Delta\ h'Es$ and $\Delta\ h_{iz}$ also demonstrate that there are some effects of the F-region MSTIDs on the E-region layers. We have also found that electric field contributed more on the Es-layers than the neutral wind (see Figures 30 - 33) in the supplementary material. We noted that the modelled and observed Es-layer altitude variations show an amplitude discrepancy. However, agreement in the time domain is very good. There are a number of sources of uncertainty associated with the modelling undertaken. These include: the HWM14 neutral wind model is a statistical empirical model. We have assumed a constant upward vertical neutral wind. The HF ray tracing relies on the statistical empirical IRI model (Kunduri et al., 2022). This directly affects the altitude of the HF ray in the F-region ionosphere and the Pedersen conductivity estimate, which both directly affect the MSTID polarisation electric field estimate.

This study showed that the vertical modulation of Es-layers were observed by a digisonde in the morning and afternoon local time over Zhongshan. At the same time, a co-located SuperDARN HF radar observed MSTIDs, of 83.8 km vertical oscillation propagating eastward (16° from east) on 04 October 2011 and of 77.0 km vertical oscillation propagating westward (8.5° from west) on 29 February 2012. Their periods were $\sim$15.0 and $\sim$12.0 min, respectively. The same periods are clearly seen in the FFT plots computed from the time series of the Es-layer virtual height (see Figures 5, 9 and 10). MSTIDs were observed in the far ranges propagating away/toward the radar, while the Es-layer was detected by the ionosonde just above the radar's location. There is a link between the Es-layer altitude modulation and the passage of MSTIDs as the two have equal periods (see periods estimated from FFT in Figures 3, 5 (A) and 9 or 4, 5 (B) and 10). Additionally, using the cross correlation between the Es-layer virtual altitude modulation and the MSTIDs backscatter power received by beam 9, we find a moderate and strong correlation of -0.46 and 0.82 implying that the MSTIDs contributed $\sim$21.2% and $\sim$67.2%, respectively on the Es-layer altitude modulations. Using co-located SuperDARN radar, ionosonde and a magnetometer data at Zhongshan, we have shown that the modulation of the observed Es-layers strongly correlate with the estimated ions velocity modulation due to different mechanisms involving the MSTIDs polarization electric field. On the other hand, instabilities generated through the Es-layers could also generate a strong polarization electric field that could produce the MSTIDs via the coupling process between the E- and F-regions (Kelley et al., 2003). The coupling between the two phenomena was also discussed by many researchers. For example in most cases, the MSTIDs are linked with the polarization electric field generated by the E-region layers (Haldoupis et al., 2003; Kelley et al., 2003; Ejiri et al., 2019), that is, the electric field would be mapped from E-region to F-region. Additional to what have been reported in this coupling process, this manuscript includes the contribution of MSTID's polarization electric field as previously reported by Otsuka et al. (2004, 2007) and Hiyadutuje et al. (2022, 2024).

6. Conclusions

To demonstrate the altitude modulation of the high-latitude Es-layers on 04 October 2011 and 29 February 2012, we analyse the Es-layer virtual height derived from ionosonde data. The total Earth's magnetic field data derived from magnetometer and MSTIDs observed in the backscatter power and modelled electric field data derived from the SuperDARN HF radar over Antarctica at Zhongshan were investigated to understand the modulation mechanism.

- A strong positive correlation between the observed Es-layer virtual altitude modulation and estimated E-region vertical ion drift modulation has been found when a Medium Scale Traveling Ionospheric Disturbance (MSTID) was propagating overhead in the F-region ionosphere. We show that the polarization electric field of MSTIDs propagating in the F-region, mapped down the near-vertical magnetic field, could contribute to the Es-layer altitude modulation via the $\mathbf{E} \times \mathbf{B}$ drift mechanism.

- Cross correlation coefficients between the Es-layer virtual heights/altitudes and MSTIDs backscatter power received by beam 9 of the Zhongshan radar show that there is a moderate and strong correlation of -0.46 and 0.82 (see Figure 5) between the two indicating that the MSTIDs contributed ~21.2% and ~67.2%, respectively on the Es-layer altitude modulations. We show that there is a strong correlation between the Es-layer virtual height modulation observed using an ionosonde and the estimated $\Delta\, h_{iz}$ using the equation involving the contribution of the MSTID's polarization electric field. To estimate h_{iz} we use the convection electric field estimated using the SuperDARN HF radars and other parameters shown in equation (4).

- Observational measurements such as the electric field in the E-region, components of neutral wind in the E- and F-region at the altitude of TIDs and very high frequency (VHF) radar are needed to accurately estimate the altitude of MSTIDs over Zhongshan to improve our results.

Declaration of competing interest

The authors declare that there is no competing financial or personal relationships with other people or organizations that could inappropriately influence (bias) this work.

Acknowledgments

The financial assistance of the National Research Foundation (NRF) (grant number: 144832) towards this research is hereby acknowledged. Opinions expressed and conclusions arrived at, are those of the authors and are not necessarily to be attributed to the NRF. This work is jointly supported by the Sino-South Africa Joint Research on Polar Space Environment (grant number: 2021YFE0106400).

The authors acknowledge the use of SuperDARN data. SuperDARN is a collection of radars funded by national scientific funding agencies of Australia, Canada, China, France, Italy, Japan, Norway, South Africa, United Kingdom and the United States of America. Thanks to the Zhongshan SuperDARN radar PI Dr Hongqiao Hu for consenting to our use of the Zhongshan data which is funded by Polar Research Institute of China. We would like to acknowledge the Chinese Meridian Project and Chinese National Polar Scientific Data Center for allowing us to use the Zhongshan radar data. The processed SuperDARN data (20111004.txt and 20120229.txt) used in the study are available at Mendeley Data via https://doi.org/10.17632/9skd2fw4yy.1 or https://data.mendeley.com/preview/9skd2fw4yy with the Creative Commons Attribution 4.0 International (CC BY 4.0) Licence that allows you to share, copy, and modify this dataset (read the licence for more information), but you may be required to register in order to access the data (Hiyadutuje et al., 2023). Alternatively, raw data can be downloaded at https://www.frdr-dfdr.ca/repo/collection/superdarn, where each year data has its own doi. SuperDARN data should be acknowledged as indicated in the acknowledgements section of this manuscript and the Principal Investigator(s) PI of the Zhongshan radar should be consulted before using the data (https://www.unis.no/project/superdarn-radar/). The SuperDARN raw data are also available from the BAS SuperDARN data mirror https://ww w.bas.ac.uk/project/superdarn/#data.

The authors would also like to acknowledge the NRLMSIS 2.0, HWM14, ionospheric conductivity, SuperDARN ray tracing and International Ionospheric (IRI) model developers.
We thank Dr Bharat.S.R Kunduri and Dr Carley Martin for their support in producing the SuperDARN ray tracing plots used in this study. Magnetometer data can be found at *http://wdc.geophys.ac.cn/*. The ZHS DPS data can be downloaded from the Data Centre for Meridian Space Weather Monitoring Project webpage (*http://data.meridianproject.ac.cn*). Magnetic Indices Data were obtained through the Kyoto and SPDF-OMNI website *https://wdc.kugi.kyoto-u.ac.jp/aedir/* (Geomagnetic Auroral Electrojet (AE) indices) and *https://omniweb.gsfc.nasa.gov/ow_min.html* (IMF data). NRLMSIS 2.0 model data are found at *https://ccmc.gsfc.nasa.gov/models/NRLMSIS* 2.0/. Zhongshan magnetometer and ionosonde data were provided by the Beijing National Observatory of Space Environment, Institute of Geology and Geophysics Chinese Academy of Sciences through the Geophysics Center, National Earth System Science Data Center (*http://wdc.geophys.ac.cn/*). The Kyto ionospheric conductivity model (height profile) is found at *https://wdc.kugi.kyoto-u.ac.jp/ionocond/exp/icexp.html*.

7. Appendix

To know, the possible altitudes of MSTIDs, we first identify which ranges the MSTIDs were observed in the figure like Figure 1 and check in the ray tracing the backscatter altitudes corresponding to those ranges. Note that the black dots indicate the altitudes and ranges where the echoes would be coming from based on the IRI and other models used in the ray tracing (Kunduri et al., 2022).

Figure 11 shows the ray tracing plots from a code initially developed by De Larquier (2013) and converted to python by Kunduri et al. (2022). Plots were generated to show the MSTIDs propagation altitude on 04 October 2011 (panel A) and 29 February 2012 (panel B). We use 10 MHz for beams 12 and 14 on 04 October 2011 and 29 February 2012, respectively of the Zhongshan HF radar. On 04 October 2011 (panel A), the backscatter power in the range ∼300 and ∼900 km came from around 200 - 300 km altitudes as shown by a 0.5 hop ionospheric scatter (see black dots of the ray tracing plot) (Kunduri et al., 2022). Echoes between 1000 and 1500 were ground scatter. On 29 February 2012 (panel B), the ray tracing plot shows that backscatter in the ranges ∼300 - ∼1200 km came from ∼100 to ∼300 km altitudes. Most of backscatter in the ranges above ∼1200 km were ground scatter. For the analysis in this study we have assumed that MSTIDs were traveling at 300 km altitude.

CRediT authorship contribution statement

Alicreance HIYADUTUJE: Conceptualization of this study, Observation, Methodology, Data analysis, Write a draft of this study. **Michael J. Kosch:** Conceptualization of this study, Methodology, Revision. **John Bosco Habarulema:** Conceptualization of this study, Methodology, Revision. **Xiangcai Chen:** Methodology, Data supply, Revision. **Judy A. E. Stephenson:** Methodology, Revision. **Tshimangadzo Merline Matamba:** Methodology, Revision. **Mpho Tshisaphungo:** Methodology.

References

Ables, S.T., Fraser, B.J., 2005. Observing the open-closed boundary using cusp-latitude magnetometers. Geophysical Research Letters 32, L10104. doi:https://doi.org/10.1029/2005GL022824.

Andoh, S., Saito, A., Shinagawa, H., Ejiri, M.K., 2020. First simulations of day-to-day variability of mid-latitude sporadic E layer structures. Earth, Planets and Space 72, 165. doi:https://doi.org/10.1186/s40623-020-01299-8.

Artru, J., Ducic, V., Kanamori, H., Lognonné, P., Murakami, M., 2005. Ionospheric detection of gravity waves induced by tsunamis. Geophysical Journal International 160, 840–848. doi:https://doi.org/10.1111/j.1365-246X.2005.02552.x.

Bernhardt, P.A., 2002. The modulation of sporadic-E layers by Kelvin–Helmholtz billows in the neutral atmosphere. Journal of atmospheric and solar-terrestrial physics 64, 1487–1504. doi:https://doi.org/10.1016/S1364-6826(02)00086-X.

Chen, X., Huang, W., Ban, C., Kosch, M.J., Murphy, D.J., Hu, Z., Liu, J., He, F., Wang, R., Yang, H., et al., 2021. Dynamic properties of a sporadic sodium layer revealed by observations over Zhongshan, Antarctica: A case study. Journal of Geophysical Research: Space Physics 126, e2021JA029787. doi:https://doi.org/10.1029/2021JA029787.

Chen, X., Liu, J., Kosch, M.J., Hu, Z., Wang, Z., Zhang, B., et al., 2022. Simultaneous observations of a sporadic E layer by Digisonde and SuperDARN HF radars at Zhongshan, Antarctica. Journal of Geophysical Research: Space Physics 127, e2021JA029921. doi:https://doi.org/10.1029/2021JA029921.

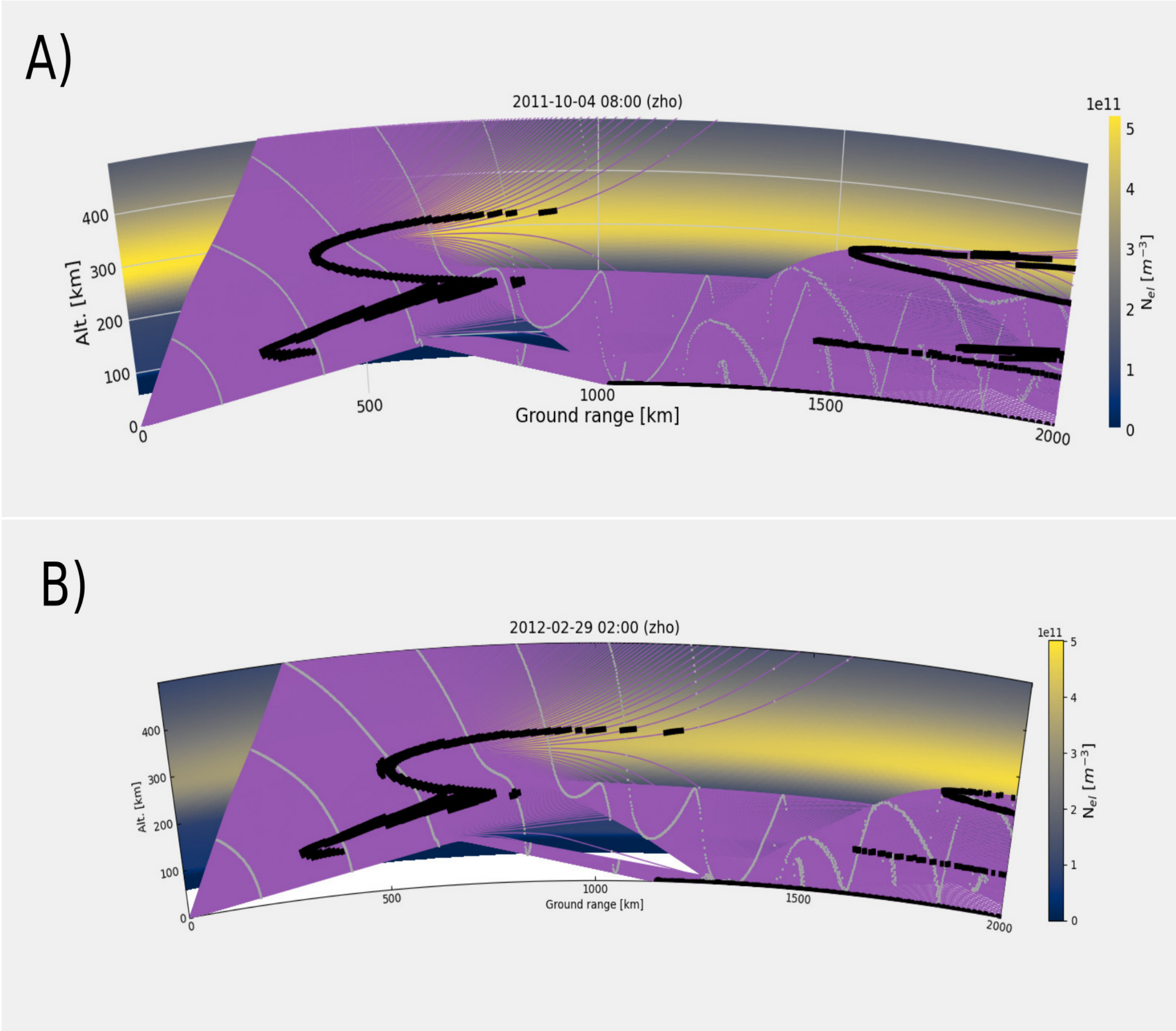

Figure 11: The ray tracing for the events on 04 October 2011 at 08:00 UT (panel A) and 29 February 2012 at 02:00 UT (panel B). MSTIDs were observed between ~500 and ~1500 km ranges.

Chen, Z., Gong, Z., Zhang, F., Fang, G., 2018. A new ionogram automatic scaling method. Radio Science 53, 1149–1164. doi:https://doi.org/10.1029/2018RS006574.

Cheng, P.H., Lin, C., Otsuka, Y., Liu, H., Rajesh, P.K., Chen, C.H., et al., 2021. Statistical study of medium-scale traveling ionospheric disturbances in low-latitude ionosphere using an automatic algorithm. Earth, Planets and Space 73, 105. doi:https://doi.org/10.1186/s40623-021-01432-1.

Chisham, G., Lester, M., Milan, S.E., Freeman, M., Bristow, W., Grocott, A., McWilliams, K., Ruohoniemi, J., Yeoman, T.K., Dyson, P.L., et al., 2007. A decade of the Super Dual Auroral Radar Network (SuperDARN): Scientific achievements, new techniques and future directions. Surveys in Geophysics 28, 33–109. doi:https://doi.org/10.1007/s10712-007-9017-8.

Clemesha, B., Batista, P., Simonich, D., 1988. Concerning the origin of enhanced sodium layers. Geophysical research letters 15, 1267–1270. doi:https://doi.org/10.1029/GL015i011p01267.

Cosgrove, R., 2007. Generation of mesoscale F layer structure and electric fields by the combined Perkins and Es layer instabilities, in simulations, in: Annales Geophysicae, Copernicus Publications Göttingen, Germany. pp. 1579–1601. doi:https://doi.org/10.5194/angeo-25-1579-2007.

Cosgrove, R.B., Tsunoda, R.T., 2004. Instability of the E-F coupled nighttime midlatitude ionosphere. Journal of Geophysical Research: Space Physics 109. doi:https://doi.org/10.1029/2003JA010243.

Cosgrove, R.B., Tsunoda, R.T., Fukao, S., Yamamoto, M., 2004. Coupling of the Perkins instability and the sporadic E layer instability derived from physical arguments. Journal of Geophysical Research: Space Physics 109. doi:https://doi.org/10.1029/2003JA010295.

Davis, C.J., Johnson, C.G., 2005. Lightning-induced intensification of the ionospheric sporadic E layer. Nature 435, 799–801. doi:https://doi.org/10.1038/nature03638.

De Larquier, S., 2013. The mid-latitude ionosphere under quiet geomagnetic conditions: Propagation analysis of SuperDARN radar observations for large ionospheric perturbations. Ph.D. thesis. Virginia Polytechnic Institute and State University.

Drob, D.P., Emmert, J.T., Meriwether, J.W., Makela, J.J., Doornbos, E., Conde, M., Hernandez, G., Noto, J., Zawdie, K.A., McDonald, S.E., et al., 2015. An update to the Horizontal Wind Model (HWM): The quiet time thermosphere. Earth and Space Science 2, 301–319. doi:https://doi.org/10.1002/2014EA000089.

Ejiri, M.K., Nakamura, T., Tsuda, T.T., Nishiyama, T., Abo, M., She, C.Y., et al., 2019. Observation of synchronization between instabilities of the sporadic E layer and geomagnetic field line connected F region medium-scale traveling ionospheric disturbances. Journal of Geophysical Research: Space Physics 124, 4627–4638. doi:https://doi.org/10.1029/2018JA026242.

Emmert, J.T., Drob, D.P., Picone, J.M., Siskind, D.E., Jones Jr, M., Mlynczak, M.G., et al., 2021. NRLMSIS 2.0: A whole-atmosphere empirical model of temperature and neutral species densities. Earth and Space Science 8, e2020EA001321. doi:https://doi.org/10.1029/2020EA001321.

Francis, S.H., 1974. A theory of medium-scale traveling ionospheric disturbances. Journal of Geophysical Research 79, 5245–5260. doi:https://doi.org/10.1029/JA079i034p05245.

Fu, W., Yokoyama, T., Ssessanga, N., Ma, G., Yamamoto, M., 2023. Nighttime Midlatitude E-F Coupling in Geomagnetic Conjugate Ionospheres: A Double Thin Shell Model and a Multi-Source Data Investigation. Journal of Geophysical Research: Space Physics 128, e2022JA031074. doi:https://doi.org/10.1029/2022JA031074.

Galkin, I.A., Reinisch, B.W., 2008. The new ARTIST 5 for all digisondes. Ionosonde Network Advisory Group Bulletin 69, 1–8.

Galushko, V., Paznukhov, V., Yampolski, Y., Foster, J., 1998. Incoherent scatter radar observations of AGW/TID events generated by the moving solar terminator, in: Annales Geophysicae, Springer Verlag Göttingen, Germany. pp. 821–827. doi:https://doi.org/10.1007/s00585-998-0821-3.

Greenwald, R., Baker, K., Dudeney, J., Pinnock, M., Jones, T., Thomas, E., Villain, J.P., Cerisier, J.C., Senior, C., Hanuise, C., et al., 1995. Darn/superdarn. Space Science Reviews 71, 761–796. doi:https://doi.org/10.1007/BF00751350.

Greenwald, R.A., Oksavik, K., Barnes, R., Ruohoniemi, J.M., Baker, J., Talaat, E.R., 2008. First radar measurements of ionospheric electric fields at sub-second temporal resolution. Geophysical Research Letters 35. doi:https://doi.org/10.1029/2007GL032164.

Grocott, A., Hosokawa, K., Ishida, T., Lester, M., Milan, S., Freeman, M., et al., 2013. Characteristics of medium-scale traveling ionospheric disturbances observed near the Antarctic Peninsula by HF radar. Journal of Geophysical Research: Space Physics 118, 5830–5841. doi:https://doi.org/10.1002/jgra.50515.

Gubenko, V., Kirillovich, I., 2019. Modulation of sporadic E layers by small-scale atmospheric waves in Earth's high-latitude ionosphere. Solar-Terrestrial Physics 5, 98–108. doi:http://doi.org/10.12737/stp-53201912.

Haldoupis, C., Haralambous, H., Meek, C., 2024. A simplified method of true height analysis to estimate the real height of sporadic E layers. Journal of Geophysical Research: Space Physics 129, e2024JA032505. doi:https://doi.org/10.1029/2024JA032505.

Haldoupis, C., Kelley, M.C., Hussey, G.C., Shalimov, S., 2003. Role of unstable sporadic-E layers in the generation of midlatitude spread F. Journal of Geophysical Research: Space Physics 108. doi:https://doi.org/10.1029/2003JA009956.

He, L.S., Dyson, P., Parkinson, M., Wan, W., 2004. Studies of medium scale travelling ionospheric disturbances using TIGER SuperDARN radar sea echo observations, in: Annales Geophysicae, pp. 4077–4088. doi:https://doi.org/10.5194/angeo-22-4077-2004.

Heale, C.J., Bossert, K., Vadas, S., Hoffmann, L., Dörnbrack, A., Stober, G., et al., 2020. Secondary gravity waves generated by breaking mountain waves over Europe. Journal of Geophysical Research: Atmospheres 125, e2019JD031662. doi:https://doi.org/10.1029/2019JD031662.

Hiyadutuje, A., Habarulema, J.B., Kosch, M.J., Chen, X., Stephenson, J., Matamba, T.M., 2023. Data on the simultaneous occurrence of Traveling Ionospheric Disturbances, Farley Buneman and Gradient Drift Instabilities observed by the Zhongshan SuperDARN HF radar. doi:https://doi.org/10.17632/9skd2fw4yy.1. data retrieved on 02/06/2022 - 25/07/2023 from the Virginia Tech website, http://vt.superdarn.org/.

Hiyadutuje, A., Habarulema, J.B., Kosch, M.J., Chen, X., Stephenson, J.A., Matamba, T.M., 2024. Simultaneous Occurrence of Traveling Ionospheric Disturbances, Farley Buneman and Gradient Drift Instabilities Observed by the Zhongshan SuperDARN HF Radar. Journal of Geophysical Research: Space Physics 129, e2023JA031367. doi:https://doi.org/10.1029/2023JA031367.

Hiyadutuje, A., Kosch, M.J., Stephenson, J.A., 2022. First Observations of E-Region Near Range Echoes Partially Modulated by F-Region Traveling Ionospheric Disturbances Observed by the Same SuperDARN HF Radar. Journal of Geophysical Research: Space Physics 127, e2021JA030157. doi:https://doi.org/10.1029/2021JA030157.

Hocke, K., Schlegel, K., et al., 1996. A review of atmospheric gravity waves and travelling ionospheric disturbances: 1982–1995. Annales Geophysicae 14, 917. doi:https://doi.org/10.1007/s00585-996-0917-6.

Huang, C.S., Kelley, M.C., 1996. Numerical simulations of gravity wave modulation of midlatitude sporadic E layers. Journal of Geophysical Research: Space Physics 101, 24533–24543. doi:https://doi.org/10.1029/96JA02327.

Hunsucker, R.D., 1982. Atmospheric gravity waves generated in the high-latitude ionosphere: A review. Reviews of Geophysics 20, 293–315. doi:https://doi.org/10.1029/RG020i002p00293.

Kelley, M.C., Haldoupis, C., Nicolls, M.J., Makela, J.J., Belehaki, A., Shalimov, S., Wong, V.K., 2003. Case studies of coupling between the E and F regions during unstable sporadic-E conditions. Journal of Geophysical Research: Space Physics 108.

doi:https://doi.org/10.1029/2003JA009955.

Kirkwood, S., Collis, P., 1989. Gravity wave generation of simultaneous auroral sporadic-E layers and sudden neutral sodium layers. Journal of atmospheric and terrestrial physics 51, 259–269. doi:https://doi.org/10.1016/0021-9169(89)90077-9.

Kirkwood, S., Nilsson, H., 2000. High-latitude sporadic-E and other thin layers–the role of magnetospheric electric fields. Space science reviews 91, 579–613. doi:https://doi.org/10.1023/A:1005241931650.

Kirkwood, S., Von Zahn, U., 1991. On the role of auroral electric fields in the formation of low altitude sporadic-E and sudden sodium layers. Journal of atmospheric and terrestrial physics 53, 389–407. doi:https://doi.org/10.1016/0021-9169(91)90034-5.

Kotake, N., Otsuka, Y., Ogawa, T., Tsugawa, T., Saito, A., 2007. Statistical study of medium-scale traveling ionospheric disturbances observed with the GPS networks in Southern California. Earth, planets and space 59, 95–102. doi:https://doi.org/10.1186/BF03352681.

Kundu, S., Chowdhury, S., Ghosh, S., Sasmal, S., Politis, D.Z., Potirakis, S.M., et al., 2022. Seismogenic anomalies in atmospheric gravity waves as observed from SABER/TIMED satellite during large earthquakes. Journal of Sensors 2022, 1–23. doi:https://doi.org/10.1155/2022/3201104.

Kunduri, B., Baker, J., Ruohoniemi, J., Thomas, E., Shepherd, S., 2022. An Examination of SuperDARN Backscatter Modes Using Machine Learning Guided by Ray-Tracing. Space Weather 20, e2022SW003130. doi:https://doi.org/10.1029/2022SW003130.

Li, H.L., Wu, J., Liu, R.Y., Huang, J.Y., 2007. Study on mesosphere summer echoes observed by digital ionosonde at Zhongshan Station, Antarctica. Earth, planets and space 59, 1135–1139. doi:https://doi.org/10.1186/BF03352056.

Li, W., Zhao, D., He, C., Shen, Y., Hu, A., Zhang, K., 2021. Application of a multi-layer artificial neural network in a 3-D global electron density model using the long-term observations of COSMIC, Fengyun-3C, and Digisonde. Space Weather 19, e2020SW002605. doi:https://doi.org/10.1029/2020SW002605.

Liu, H.L., Hagan, M.E., Roble, R.G., 2000. Local mean state changes due to gravity wave breaking modulated by the diurnal tide. Journal of Geophysical Research: Atmospheres 105, 12381–12396. doi:https://doi.org/10.1029/1999JD901163.

Liu, Y., Hu, H., Yang, H., Zhang, B., Sun, B., Wei, F., et al., 2016. Chinese Antarctic magnetometer chain at the cusp latitude. Advances in Polar Science 27, 102–106. doi:https://doi.org/10.13679/j.advps.2016.2.00102.

Liu, Y., Zhou, C., Xu, T., Tang, Q., Deng, Z., Chen, G., Wang, Z., 2021. Review of ionospheric irregularities and ionospheric electrodynamic coupling in the middle latitude region. Earth and Planetary Physics 5, 462–482. doi:http://doi.org/10.26464/epp2021025.

MacDougall, J., Jayachandran, P., Plane, J., 2000. Polar cap sporadic-E: part 1, observations. Journal of Atmospheric and Solar-Terrestrial Physics 62, 1155–1167. doi:https://doi.org/10.1016/S1364-6826(00)00093-6.

Mathews, J., 1998. Sporadic E: current views and recent progress. Journal of atmospheric and solar-terrestrial physics 60, 413–435. doi:https://doi.org/10.1016/S1364-6826(97)00043-6.

Mikumo, T., Shibutani, T., Le Pichon, A., Garces, M., Fee, D., Tsuyuki, T., et al., . Low-frequency acoustic-gravity waves from coseismic vertical deformation associated with the 2004 Sumatra-Andaman earthquake (Mw= 9.2) .

Miyoshi, Y., Jin, H., Fujiwara, H., Shinagawa, H., 2018. Numerical study of traveling ionospheric disturbances generated by an upward propagating gravity wave. Journal of Geophysical Research: Space Physics 123, 2141–2155. doi:https://doi.org/10.1002/2017JA025110.

Narayanan, V., Shiokawa, K., Otsuka, Y., Neudegg, D., 2018. On the role of thermospheric winds and sporadic e layers in the formation and evolution of electrified MSTIDs in geomagnetic conjugate regions. Journal of Geophysical Research: Space Physics 123, 6957–6980. doi:https://doi.org/10.1029/2018JA025261.

Ogawa, T., Sekito, N., Nozaki, K., Yamamoto, M., 1998. Height comparison of midlatitude E region field-aligned irregularities and sporadic E layer. Geophysical research letters 25, 1813–1816. doi:https://doi.org/10.1029/98GL00864.

Otsuka, Y., 2021. Medium-scale traveling ionospheric disturbances. Ionosphere dynamics and applications , 421–437doi:https://doi.org/10.1002/9781119815617.ch18.

Otsuka, Y., Onoma, F., Shiokawa, K., Ogawa, T., Yamamoto, M., Fukao, S., 2007. Simultaneous observations of nighttime medium-scale traveling ionospheric disturbances and E region field-aligned irregularities at midlatitude. Journal of Geophysical Research: Space Physics 112. doi:https://doi.org/10.1029/2005JA011548.

Otsuka, Y., Shiokawa, K., Ogawa, T., Wilkinson, P., 2004. Geomagnetic conjugate observations of medium-scale traveling ionospheric disturbances at midlatitude using all-sky airglow imagers. Geophysical research letters 31. doi:https://doi.org/10.1029/2004GL020262.

Otsuka, Y., Shiokawa, K., Ogawa, T., Yokoyama, T., Yamamoto, M., 2009. Spatial relationship of nighttime medium-scale traveling ionospheric disturbances and F region field-aligned irregularities observed with two spaced all-sky airglow imagers and the middle and upper atmosphere radar. Journal of Geophysical Research: Space Physics 114. doi:https://doi.org/10.1029/2008JA013902.

Otsuka, Y., Tani, T., Tsugawa, T., Ogawa, T., Saito, A., 2008. Statistical study of relationship between medium-scale traveling ionospheric disturbance and sporadic E layer activities in summer night over Japan. Journal of Atmospheric and Solar-Terrestrial Physics 70, 2196–2202. doi:https://doi.org/10.1016/j.jastp.2008.07.008.

Pancheva, D., Haldoupis, C., Meek, C., Manson, A., Mitchell, N., 2003. Evidence of a role for modulated atmospheric tides in the dependence of sporadic E layers on planetary waves. Journal of Geophysical Research: Space Physics 108. doi:https://doi.org/10.1029/2002JA009788.

Pashin, A., Belova, E., Lyatsky, W., 1995. Magnetic pulsation generation by a powerful ground-based modulated HF radio transmitter. Journal of Atmospheric and Terrestrial Physics 57, 245–252. doi:https://doi.org/10.1016/0021-9169(93)

E0005-T.
Paulino, I., Medeiros, A.F., Vadas, S., Wrasse, C.M., Takahashi, H., Buriti, R., et al., 2016. Periodic waves in the lower thermosphere observed by OI630 nm airglow images, in: Annales Geophysicae, Copernicus Publications Göttingen, Germany. pp. 293–301. doi:https://doi.org/10.5194/angeo-34-293-2016.
Qiu, S., Wang, N., Soon, W., Lu, G., Jia, M., Wang, X., et al., 2021. The sporadic sodium layer: a possible tracer for the conjunction between the upper and lower atmospheres. Atmospheric Chemistry and Physics 21, 11927–11940. doi:https://doi.org/10.5194/acp-21-11927-2021.
Rathi, R., Yadav, V., Mondal, S., Sarkhel, S., Sunil Krishna, M., Upadhayaya, A., Kannaujiya, S., Chauhan, P., 2022. A Case Study on the Interaction Between MSTIDs' Fronts, Their Dissipation, and a Curious Case of MSTID's Rotation Over Geomagnetic Low-Mid Latitude Transition Region. Journal of Geophysical Research: Space Physics 127, e2021JA029872. doi:https://doi.org/10.1029/2021JA029872.
Rees, D., Smith, R., Charleton, P., McCormac, F., Lloyd, N., Steen, Å., 1984. The generation of vertical thermospheric winds and gravity waves at auroral latitudes—I. Observations of vertical winds. Planetary and space science 32, 667–684. doi:https://doi.org/10.1016/0032-0633(84)90092-8.
Resende, L., Zhu, Y., Denardini, C., Chagas, R., Da Silva, L., Andrioli, V., et al., 2023. Analysis of the different physical mechanisms in the atypical sporadic E (Es) layer occurrence over a low latitude region in the Brazilian sector. Frontiers in Astronomy and Space Sciences 10, 1193268. doi:https://doi.org/10.3389/fspas.2023.1193268.
Ripepe, M., De Angelis, S., Lacanna, G., Voight, B., 2010. Observation of infrasonic and gravity waves at Soufrière Hills Volcano, Montserrat. Geophysical Research Letters 37. doi:https://doi.org/10.1029/2010GL042557.
Ruohoniemi, J., Baker, K., 1998. Large-scale imaging of high-latitude convection with Super Dual Auroral Radar Network HF radar observations. Journal of Geophysical Research: Space Physics 103, 20797–20811. doi:https://doi.org/10.1029/98JA01288.
Ruohoniemi, J., Greenwald, R., 1996. Statistical patterns of high-latitude convection obtained from Goose Bay HF radar observations. Journal of Geophysical Research: Space Physics 101, 21743–21763. doi:https://doi.org/10.1029/96JA01584.
Schunk, R., Nagy, A., 2009. Ionospheres: physics, plasma physics, and chemistry. Cambridge university press.
Shalimov, S., Kozlovsky, A., 2015. High-latitude E and F region coupling signature: A case study results from rapid-run ionosonde. Journal of Geophysical Research: Space Physics 120, 3033–3041. doi:https://doi.org/10.1002/2014JA020589.
Shepherd, S., Ruohoniemi, J., 2000. Electrostatic potential patterns in the high-latitude ionosphere constrained by SuperDARN measurements. Journal of Geophysical Research: Space Physics 105, 23005–23014. doi:https://doi.org/10.1029/2000JA000171.
Shinbori, A., Otsuka, Y., Sori, T., Nishioka, M., Perwitasari, S., Tsuda, T., Nishitani, N., 2022. Electromagnetic conjugacy of ionospheric disturbances after the 2022 Hunga Tonga-Hunga Ha'apai volcanic eruption as seen in GNSS-TEC and SuperDARN Hokkaido pair of radars observations. Earth, Planets and Space 74, 1–17. doi:https://doi.org/10.1186/s40623-022-01665-8.
Sieradzki, R., Paziewski, J., 2015. Mstids impact on GNSS observations and its mitigation in rapid static positioning at medium baselines. Annals of Geophysics 58, A0661–A0661. doi:https://doi.org/10.4401/ag-6891.
Sivakandan, M., Martinis, C., Otsuka, Y., Chau, J.L., Norrell, J., Mielich, J., et al., 2022. On the Role of E-F Region Coupling in the Generation of Nighttime MSTIDs During Summer and Equinox: Case Studies Over Northern Germany. Journal of Geophysical Research: Space Physics 127, e2021JA030159. doi:https://doi.org/10.1029/2021JA030159.
Snively, J.B., Pasko, V.P., 2003. Breaking of thunderstorm-generated gravity waves as a source of short-period ducted waves at mesopause altitudes. Geophysical Research Letters 30. doi:https://doi.org/10.1029/2003GL018436.
Swartz, W., Kelley, M., Aponte, N., 2009. E-and F-region coupling between an intense sporadic E layer and a mesoscale traveling ionospheric disturbance, in: Annales geophysicae, Copernicus Publications Göttingen, Germany. pp. 2475–2482. doi:https://doi.org/10.5194/angeo-27-2475-2009.
Thaganyana, G.P., Habarulema, J.B., Ngwira, C., Azeem, I., 2022. Equatorward Medium to Large-Scale Traveling Ionospheric Disturbances of High Latitude Origin During Quiet Conditions. Journal of Geophysical Research: Space Physics 127, e2021JA029558. doi:https://doi.org/10.1029/2021JA029558.
Thomas, E.G., Shepherd, S.G., 2018. Statistical patterns of ionospheric convection derived from mid-latitude, high-latitude, and polar SuperDARN HF radar observations. Journal of Geophysical Research: Space Physics 123, 3196–3216. doi:https://doi.org/10.1002/2018JA025280.
Tsunoda, R.T., Cosgrove, R.B., 2001. Coupled electrodynamics in the nighttime midlatitude ionosphere. Geophysical Research Letters 28, 4171–4174. doi:https://doi.org/10.1029/2001GL013245.
Tsunoda, R.T., Fukao, S., Yamamoto, M., 1994. On the origin of quasi-periodic radar backscatter from midlatitude sporadic E. Radio Science 29, 349–365. doi:https://doi.org/10.1029/93RS01511.
Van Eaton, A.R., Lapierre, J., Behnke, S.A., Vagasky, C., Schultz, C.J., Pavolonis, M., et al., 2023. Lightning rings and gravity waves: Insights into the giant eruption plume from Tonga's Hunga Volcano on 15 January 2022. Geophysical Research Letters 50, e2022GL102341. doi:https://doi.org/10.1029/2022GL102341.
Von Zahn, U., Hansen, T., 1988. Sudden neutral sodium layers: A strong link to sporadic E layers. Journal of Atmospheric and Terrestrial Physics 50, 93–104. doi:https://doi.org/10.1016/0021-9169(88)90047-5.
Wahlund, J.E., Opgenoorth, H., 1989. EISCAT observations of strong ion outflows from the F-region ionosphere during auroral activity: Preliminary results. Geophysical Research Letters 16, 727–730. doi:https://doi.org/10.1029/GL016i007p00727.
Wahlund, J.E., Opgenoorth, H., Rothwell, P., 1989. Observations of thin auroral ionization layers by EISCAT in connection with pulsating aurora. Journal of Geophysical Research: Space Physics 94, 17223–17233. doi:https://doi.org/10.1029/

JA094iA12p17223.

Woodman, R., Yamamoto, M., Fukao, S., 1991. Gravity wave modulation of gradient drift instabilities in mid-latitude sporadic E irregularities. Geophysical Research Letters 18, 1197–1200. doi:https://doi.org/10.1029/91GL01159.

Yenen, S., Gulyaeva, T., Arikan, F., Arikan, O., 2015. Association of ionospheric storms and substorms of Global Electron Content with proxy AE index. Advances in Space Research 56, 1343–1353. doi:https://doi.org/10.1029/2010JA015866.

Yin, F., Lühr, H., Park, J., Wang, L., 2019. Comprehensive analysis of the magnetic signatures of small-scale traveling ionospheric disturbances, as observed by Swarm. Journal of Geophysical Research: Space Physics 124, 10794–10815. doi:https://doi.org/10.1029/2019JA027523.

Yokoyama, T., Horinouchi, T., Yamamoto, M., Fukao, S., 2004. Modulation of the midlatitude ionospheric E region by atmospheric gravity waves through polarization electric field. Journal of Geophysical Research: Space Physics 109. doi:https://doi.org/10.1029/2004JA010508.

Yokoyama, T., Hysell, D.L., Otsuka, Y., Yamamoto, M., 2009. Three-dimensional simulation of the coupled Perkins and Es-layer instabilities in the nighttime midlatitude ionosphere. Journal of Geophysical Research: Space Physics 114. doi:https://doi.org/10.1029/2008JA013789.

Yokoyama, T., Otsuka, Y., Ogawa, T., Yamamoto, M., Hysell, D.L., 2008. First three-dimensional simulation of the Perkins instability in the nighttime midlatitude ionosphere. Geophysical research letters 35. doi:https://doi.org/10.1029/2007GL032496.

Zhang, S.R., Oliver, W., Fukao, S., 2001. MU radar ion drift model. Advances in Space Research 27, 115–120. doi:https://doi.org/10.1016/s0273-1177(00)00146-0.

Zhang, Y., Paxton, L.J., 2021. Space Physics and Aeronomy, Ionosphere Dynamics and Applications. John Wiley & Sons.